CFD modelling of Close-Coupled Gas Atomisation (CCGA) process by employing the Euler-Lagrange approach to understand melt flow instabilities

Jo Samuel J [a],[*], Andrew M. Mullis [a], Duncan J. Borman [b]

[a] *School of Chemical and Process Engineering, University of Leeds, Leeds LS2 9JT, UK*
[b] *School of Civil Engineering, University of Leeds, Leeds LS2 9JT, UK*

ABSTRACT

This paper presents a CFD analysis of the melt and flow-field instabilities in a close-coupled gas atomisation process (CCGA) caused by the gas–melt interactions. The melt mass flow is coupled to the atomiser internal pressure, which varies over time due to the unsteady flow field. A two-phase flow of Argon gas and melt particles is modelled using a coupled Euler-Lagrange framework. Three different initial gas-to-melt ratios (GMRs) of 5.5, 2.6 and 1.32 are considered to study the gas–melt interaction. The results show that in the case GMR = 1.32, sustained instability both in the melt and in the flow-field are distinctly observed, resembling physical atomisation process. This melt fluctuation corresponded to an alternating flow-field fluctuation; alternating between open- to closed-wake condition, where the local maxima of the melt corresponded to an open-wake condition, and the local minima of the melt corresponded to a closed-wake condition.

1. Introduction

Over the past few decades, powder metallurgy has gained popularity within the manufacturing industry due to its extensive use in producing intricate products spanning from small-scale dimensions to significantly larger objects. Achieving similar scale and intricacy using conventional manufacturing methods is not often feasible (Amatriain et al., 2022). Multiple methods and processes have been developed for metal powder production. However, the High Pressure Gas Atomisation (HPGA) process is at the forefront, producing particles smaller than 50 μm which are of high in quality, purity and sphericity (Ünal & Aydin, 2007, Zeoli and Gu, 2006). Gas atomisation illustrated in Fig. 1a, uses the principle of converting the kinetic energy of a high-speed gas-jet to disintegrate a molten metal stream, and simultaneously solidifying it, producing, fine metal powders (Buelow, 2005, Wang et al., 2024). The high-pressure gas-jet exiting the gas nozzle (convergent, cylindrical, and convergent-divergent nozzle) rapidly expands downstream, forming a supersonic flow, with typical characteristics flow features such as oblique shocks, expansion waves, recompression shocks, and Mach-disk. Owing to the symmetrical arrangement of the gas jets, by virtue of the flow, there is a recirculation zone formed in front of the melt nozzle. This recirculation zone forces the melt to flow over the melt nozzle tip before flowing downstream, in a process known as pre-filming (Zeoli and Gu, 2008) as illustrated in Fig. 1b. As a result of the recirculation zone an aspiration pressure is induced just in front of the melt nozzle which pulls the melt from the tundish (Anderson et al., 1991). However, the underlying physics of the process is poorly understood. The process is challenging to investigate due to the combined effects of the chaotic nature and harsh environmental conditions; complexities in the melt flow caused by the gas–melt interactions; and lengthy working distance (Wang et al., 2023). Moreover, the process of a liquid droplet transitioning from its liquid state to a solid metal powder occurs incredibly quickly—in the order of milliseconds, mirroring the instability of the process (Mullis et al., 2013b, Zhao et al., 2009).

To understand this process Ting, 2003 postulated a theory, providing a sequence of flow–field phenomena that can occur, giving rise to this unstable process. At high operating pressure as used in a typical gas atomisation process, a Mach-disk is observed in the flow-field just below the melt nozzle outlet, as shown in Fig. 2. The region in the flow-field present in front of the melt nozzle outlet, i.e. the region bordered by the inner sonic boundary radially and the Mach-disk downstream, is known as the wake, shown in Fig. 1c. The operating pressure at which the Mach-disk is observed is called the Wake-Closure Pressure (WCP). The presence or absence of a Mach-disk indicates whether the wake is in

---

* Corresponding author.
E-mail addresses: pmjsjs@leeds.ac.uk (J. Samuel J), a.m.mullis@leeds.ac.uk (A.M. Mullis), d.j.borman@leeds.ac.uk (D.J. Borman).

closed- or open-wake condition, respectively (Motaman et al., 2015). Ting's postulated sequence of events start with the melt entering and accumulating in the wake-region whilst it is in closed–wake condition. The melt accumulation ruptures the Mach-disk with a sudden burst leading to open-wake condition. Immediately after this rupture, once again the Mach disk is re-established, re-entering into closed-wake condition. This flow-field transition from closed–wake to open-wake condition keeps alternating, resulting in fluctuating aspiration pressure, which give rise to rapid changes in the mass flow rate and in-turn to the gas-to-melt ratio (GMR)[1] over short time-scales. It was estimated that the GMR varied by a factor of 12 over a period of 3.64 s (Mullis et al., 2013a). It was also estimated that this fluctuation is around 25–50 Hz (Mullis et al., 2007). This chaotic nature gives rise to larger particle size as well as to increased particle size distribution. Considering the particles are distributed log-normally with a standard deviation, σ_{LN} = 2.0, the typical yields for a size fraction of 38 – 75 µm is only 35 %, with the remainder of the out-of-specification powder generally being remelted in a subsequent batch of atomisation (Yule and Dunkley, 1994). This substantially increases both the capital and energy expenditure, making the process very inefficient (Luo et al., 2023).

With the recent advancements in the computing resources, significant progress has been made in the analysis of the gas atomisation process using computational fluid dynamics (CFD) modelling. Multiple CFD studies have shown that a standalone gas–only flow simulation is in good agreement with the experimentally observed behaviour of atomisers run in gas-only flow. The process has also been modelled as two-phase flows both using the Euler-Euler (E-E) and the Euler-Lagrange (E-L) Framework. The former approach involves modelling of each phase as a continuum, whereas the latter approach is mostly used to analyse the particles' dimensional and thermal properties. The E-L framework is typically more computationally tractable, so can simulate longer durations of the gas atomisation process (Guo et al., 2020, Luo et al., 2021, Shi et al., 2022). The E-L model is widely adopted in modelling the gas atomisation process and hence is focussed for the rest of this paper. Kaiser et al. (2018), employing the E-L approach, also

known as Discrete-Phase model (DPM), along with Kelvin-Helmholtz (KH) breakup model investigated the effect on particles using two different gas nozzles: annular silt nozzle (ASN) and isentropic plug nozzle (IPN). It was found when using IPN, the flow-field possessed higher energy, which interpreted into higher weber number than the ASN, resulting in better atomisation. The mass median diameter (MMD) was evaluated to be 45 µm for the IPN while it was 52 µm for the ASN. The numerical simulation corroborated with the experimental work carried out by Luo et al. (2023) wherein the increase in gas pressure, indicating higher weber number resulted in progressive decrease in droplet size during primary break-up. Similarly, in another numerical study Xu et al. (2020) used DPM model to investigate the particle breakup. The study used two breakup models: Kelvin-Helmholtz Rayleigh-Transport (KHRT) breakup model for outside the liquid core and WAVE breakup model for within liquid core. A number of parameters including gas temperature, half tapered angle (β), protrusion length (δ) and gas slit diameter (d_j) were varied to attempt to understand the atomisation process and its effect on particle size. The results concluded with the increase in gas jet temperature finer particles were obtained. Similarly, an increase in protrusion length to an optimum length of 4 mm was seen to improve atomisation, whereas lengths beyond that, resulted in coarser particles. Likewise, modification to system configuration as demonstrated in a study conducted out by Wang et al. (2024) wherein installation of an additional gas nozzle to the existing configuration, led to a significant 34 % increase in the yield of finer particles.

In a study carried out by Ashokkumar (2020) the gas–melt interactions and the particle trajectories were analysed in the supersonic flow–field by employing the DPM model. The study used a constant mass flow rate of particles with a fixed particle size of 500 µm at a temperature of 300 K. From the above study, the presence of a fluctuating aspiration pressure was observed due to the gas-melt interactions. Nevertheless, full coupling between aspiration pressure and melt flow in a fully coupled atomisation system has not yet been investigated. In this research, using the E-L approach, the coupling between the aspiration pressure and the melt flow rate is studied. The study will provide means
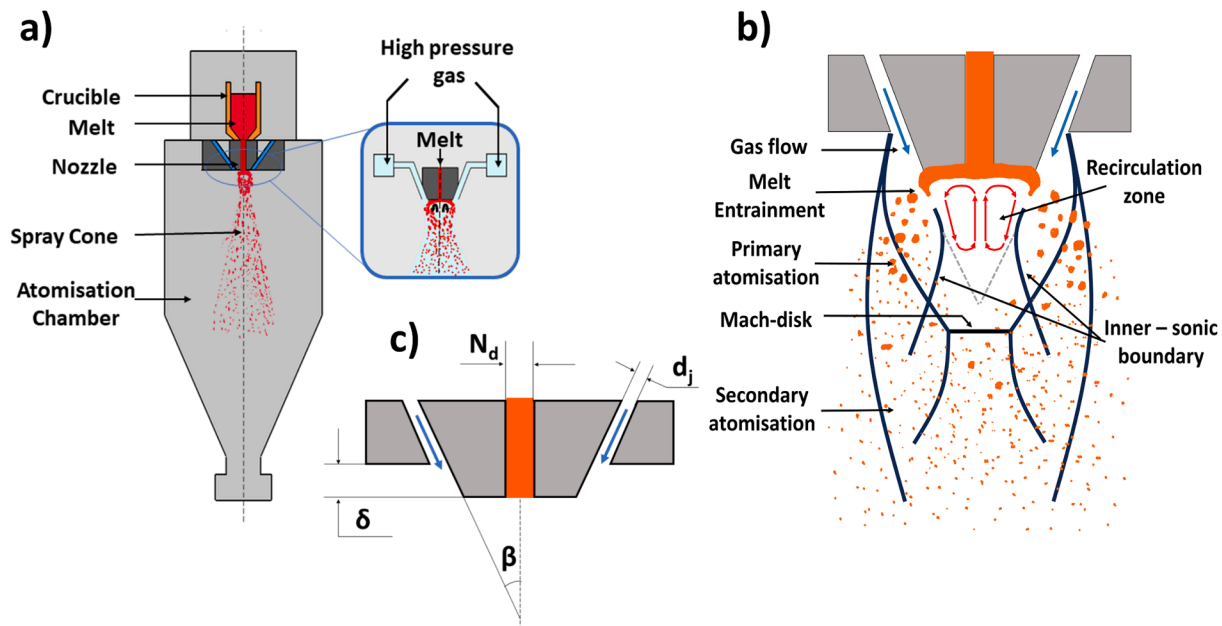

Fig. 1. Schematic illustration of the (a) gas-atomization set-up, (b) close-coupled atomizer illustrating pre-filming, and (c) melt nozzle with their dimensions.

---

[1] GMR is the ratio of mass flow rate of the gas to the mass flow rate of the melt.

to further understand and confirm the pulsation hypothesis proposed by Ting, and will provide deeper understanding on the gas–melt interactions around the wake region and downstream. This research is also a first step towards a full process model for process optimisation and

elimination of instabilities.

2. Fluid modelling

In this paper, using ANSYS Fluent v19.2 Finite Volume Method (FVM) based CFD code, an annular-slit gas atomiser is modelled as a 2D axisymmetric model owing to the symmetry about the atomiser's axis. The primary phase – gas (Argon) is modelled as a compressible unsteady flow using Reynolds Averaged Navier–Stokes (RANS) equation. The energy equation is employed and solved; the turbulent gas flow is modelled using $k - \omega$ standard turbulence model since it has reliably been shown to well predicted the flow, whereas $k - \varepsilon$ and $k - \omega \; SST$ models have been shown in some situation underpredicted the flow velocity and have failed to develop Mach disk seen at higher pressure (Motaman et al., 2013).

Since the melt becomes droplets (particles) during primary atomisation (Duangkhamchan et al., 2012), and that the present research focuses on the coupling between the melt flow rate and the aspiration pressure, rather than explicitly attempting to resolve the highly complex melt breakup, the secondary phase i.e. melt, is considered as discrete particles and modelled using the E-L approach. The particles are modelled using the DPM model, which uses the fully two-way coupled E-L approach to compute the particle trajectories resulting from the coupled interaction of gas with particles and vice-versa. The E–L approach is adopted in this study to make the simulation computationally tractable and facilitate longer simulation runs. The Lagrangian particles are considered to be inert, constant diameter, and spherical in shape. The particle's trajectory is predicted by force balance wherein the particle's inertia and forces acting on it are equated as seen in the equation (1),

$$ m_P \frac{d\vec{u}_P}{dt} = m_p \frac{\vec{u} - \vec{u}_p}{\tau_r} + \vec{F} \tag{1} $$

$$ \tau_r = \frac{\rho_p d_p^2}{18\mu} \frac{24}{C_d Re} \tag{2} $$

$$ Re \equiv \frac{\rho_p d_p \left| \vec{u} - \vec{u}_p \right|}{\mu} \tag{3} $$

where, $m_p \frac{\vec{u} - \vec{u}_p}{\tau_r}$ is the drag force acting on the particle, $\vec{F}$ is any other additional forces acting on the particle, m_p is the mass of the particle, τ_r is the droplet relaxation time defined in equation (2), Re is the relative Reynolds number defined in equation (3), C_d is the drag coefficient, $\vec{u}_p$ is the particle velocity, ρ_p is the density of the particle, μ is the molecular viscosity and d_p is the diameter of the particle. Gravity is not taken account into this model.

The mass flow rate of the secondary phase is coupled with the measured aspiration pressure by employing an User Defined Function (UDF) via ANSYS fluent. The code is compiled so as to load it as a library file thereby making it a part of ANSYS Fluent executable. The flow variable considered for coupling is pressure, since the aspiration pressure controls the mass flow rate entering into the atomising chamber as explained earlier. A monitor is setup just in front of the melt nozzle as shown in the Fig. 3, covering the region where the aspiration pressure exists, and is recorded for every timestep. The mass flow rate ($\dot{m}$) is proportional to the aspiration pressure (A_{sp}), and to match the experimentally observed flow rates in a physical atomiser, as carried out by Mullis et al. (2007) and McCarthy et al. (2013), a proportionality
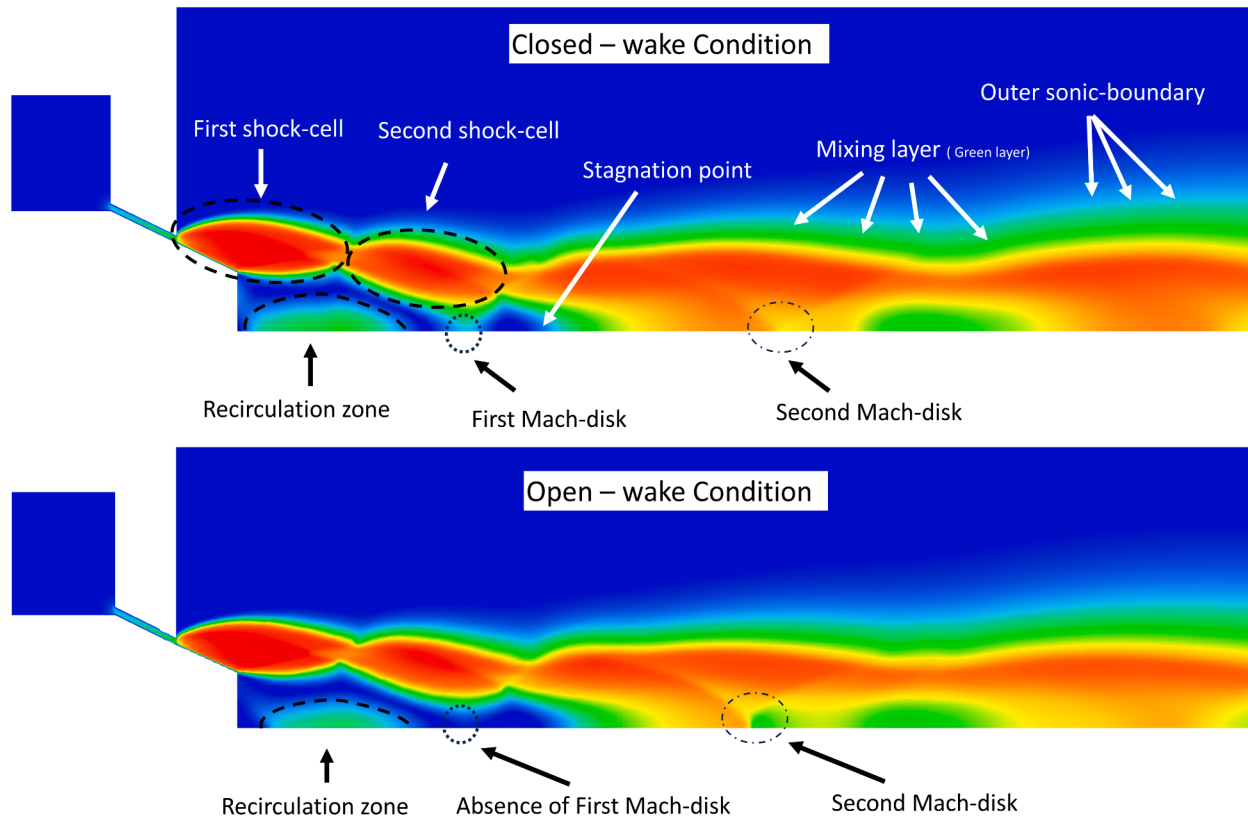

Fig. 2. Velocity contour of the gas flow-field showing characteristics flow features such as shock-cells, stagnation point, recirculation zone, and Mach-disks. The flow-field is said to be in closed-wake condition when the first Mach-disk i.e. the Mach-disk present in close proximity to the melt nozzle outlet is significantly observed. Conversely, in the absence of the first Mach-disk, the gas flow-field exists in open-wake condition. The scale for the velocity contour is not presented as this figure is for illustration.
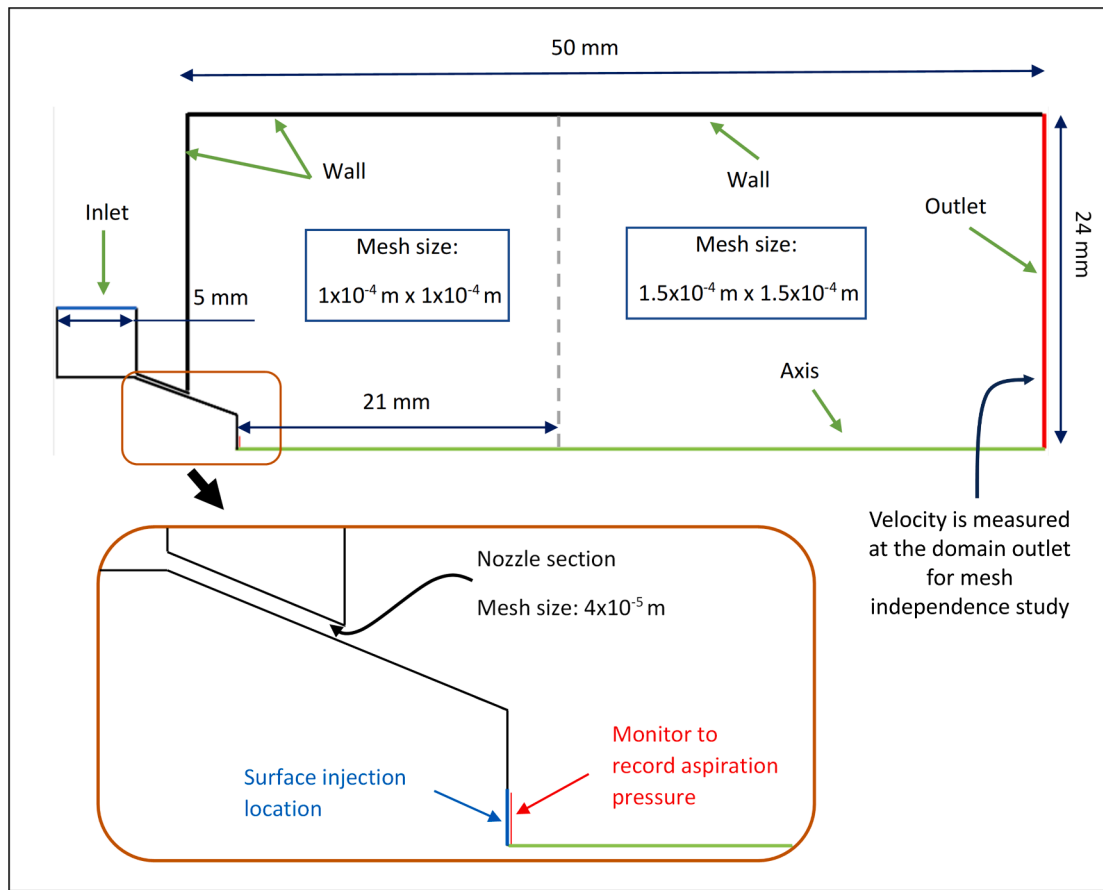
Fig. 3. Modelling domain with zoomed-in gas nozzle section presented with finest mesh size. The geometry is divided into two sections using the dashed grey line interface at a distance of 21 mm from the melt nozzle exit. Excluding the nozzle section, the section to left of the interface is meshed with a minimum mesh size of 1×10^{-4} m, and for the section to the right a minimum mesh size of 1.5×10^{-4} m is used.

constant (K) is used, as presented in the equation (4).

$$\dot{m} = K*A_{sp} \qquad (4)$$

The proportionality constant is calculated based on the estimated A_{sp} determined in gas only flow. Usually, in the physical atomisation process an over-pressure is applied to the melt to prevent it from melt freeze-off, and to replicate the experimental process, an over-pressure of 50 kPa is considered for this model. In equation (4), the aspiration pressure is computed by combining the estimated initial aspiration pressure and the over-pressure, which comes out to be 75 kPa, giving $K = 3.2 \times 10^{-7}$ kg s^{-1} Pa^{-1}.

2.1. Model implementation

The 2D axisymmetric model's computational domain presented in Fig. 3 shows the geometrical extents of the domain and its boundary conditions. As mentioned in the previous section, Argon, an ideal gas, is selected as the working fluid, and solved for continuity, momentum, and energy equations. Since, the flow is modelled as a compressible flow, density is solved using the compressible ideal-gas law equation. The simulation was run as a density-based second order formulation model.

The melt delivery tube is eliminated and replaced with a wall where the DPM particles are injected. As in the physical gas atomisation process, the working fluid, Argon, will not enter into the melt delivery tube from the atomisation chamber. The temperature of the gas is set to 300 K and an inlet operating pressure of 4.5 MPa is used so as to run the model under closed-wake condition. This operating pressure was determined after carrying out preliminary gas only flow simulations at different

operating pressures. A very small timestep size of 5×10^{-8} s is required for this coupled multiphase flow simulation. This was empirically determined as the largest timestep under which simulation results were stable and insensitive to further reductions in step-size. To ensure good solution convergence, and avoid any numerical instability, the residuals and mass imbalances were monitored. The residuals' tolerances were found to be consistently below 1×10^{-4} for continuity and x-velocity; 1×10^{-5} for y-velocity; and 1×10^{-7} for energy. Also, the mass imbalance was observed to be less than 1 %.

The secondary DPM phase is employed via surface injection at the melt nozzle exit, as shown in Fig. 3. The atomiser design is adopted from Mullis et al. (2007), McCarthy et al. (2013), wherein the preferred nozzle diameter (N_d) is 2 mm and the melt used is Ni-50wt%Al. Hence the same is adopted for this study. The average mass flow rate of the injection for the above–mentioned N_d (Fig. 1c) is determined based an experimental setup run on research-scale atomiser. The corresponding injection velocity is calculated based on an estimate of the actual velocity of the melt in the 2 mm bore nozzle. From the density of the melt (ρ_{melt}) and the mass flow rate the volumetric flow rate is found. Using the volumetric flow rate and the cross-sectional area (A) of the nozzle bore, the injection velocity (u_{melt}) of the particles is calculated. As presented in equation (5) the velocity was found to be 1.38 m s^{-1}.

$$u_{melt} = \frac{\dot{m}}{\rho_{melt}*A} = \frac{0.0166}{3850*\pi*0.001^2} = 1.38 ms^{-1} \qquad (5)$$

Even though the size of metal powders obtained from the atomisation process varies between 15 and 500 μm (Ashokkumar, 2020; Anderson et al., 2018), for this work the particles are modelled as a constant-diameter particle of 500 μm. This diameter is considered so as

to reduce the computational load and at the same time utilise particle size that is within the yield size range i.e. 15–500 μm. With the decrease in particle size, there would be an increase in number of tracked particles within the domain, correspondingly leading to an increased computational load and longer run-time. Moreover, particle size of 500 μm is employed, as that's the order of size of the particles existing in the primary atomisation zone, and this will be supplementing towards understanding of the gas–melt interactions in the wake region more specifically. The particles are considered to be inert and are maintained at a temperature of 300 K. To understand the interaction between gas and the melt, two–way coupling is employed along with Discrete Random Walk (DRW) model. Since, the velocity and trajectory of the particles within the gas flow will be determined by the nature of the drag force upon those droplets, in this work spherical drag law that scales based upon the Reynolds number approximation of Morsi and Alexander (1972) is employed. With the shape and diameter of the particle fixed, C_d remains constant. Also, in order to ensure the model accurately reflects actual atomization process, the magnitude of the drag force is set so as to reflect typical velocities actually observed in atomization melt plume. For this purpose, we refer to the work of Bigg & Mullis (Bigg and Mullis, 2020), who used a statistical image tracking technique to map velocities within an atomization plume, finding that these varied from a few metres per second in the plume centre to a few tens of metres per second on the plume margins, where the interaction of the gas and melt is strongest. Allowing for a slight underestimation of velocity in the work of Bigg & Mullis, due to loss of tracking as the particles cool (personal communication) and that the atomizing gas pressure used in this present study is more than twice that in the study by Bigg & Mullis, we believe that the measured melt velocities of around 70 ms^{-1} on the plume margins are realistic for the atomisation conditions prevailing, validating the drag model that is employed.

A mesh independence study was carried out with four different mesh resolutions and were analysed on gas-only flow-field. 13,000, 60,000, 110,000 and 170,430 elements, whose smallest element sizes were 1.2x10^{-4} m, 6x10^{-5} m, 4x10^{-5} m and 3x10^{-5} m, respectively, were generated for the same domain to carry out the mesh independence study. The difference in the velocities for 110,000 and 170,430 elements at the outlet of the domain (Fig. 3) were negligible as shown in the Fig. 4, hence the mesh having total number of elements of 110,000 was chosen to carry out the rest of the simulation study.

A gas-only flow simulation was run with the above finalised mesh. It was observed, the simulation reached a steady flow velocity without any significant changes at 20 ms, indicating the flow has achieved a steady-state. The model was then run for another 10 ms i.e. up to 30 ms to ensure the flow continues to exist in steady-state and is numerically stable prior to the introduction of the second phase.

A DPM sensitivity study was carried out using different particle size, but of constant mass flow rate of 0.016 kg s^{-1}, to analyse the effects of particle mass on the gas flow and particle trajectory. Three different

Fig. 4. Mesh independency study showing 110,000 elements is optimum in carrying out the simulation.

particle sizes were considered and were run for 20 ms (from 30 ms to 50 ms). The considered particle sizes were 390 μm, 500 μm and 610 μm. The flow-field in each of the simulation were investigated for changes taking place at the mid-domain and at the outlet. The results were in close agreement within tolerances. With flow-field being insensitive to 390 μm particle size, no further smaller size particles were simulated in the DPM sensitivity study, owing to high computational cost. Also, another DPM study was carried out using DRW model to observe the melt dispersion alongside with the gas–melt interaction. A DPM model having a constant mass flow rate of 0.016 kg s^{-1} was run with and without stochastic random walk model using the DRW model, from 30 ms to 100 ms. When the particle trajectories were examined, it was clear that they were different, and that stochastic random walk model leads to more dispersion of particles as it moves downstream as shown in Fig. 5. Since, the observed distribution of particles agrees better with the experimentally observed melt plume as captured by high-speed filming, DRW model is employed for rest of the simulation.

2.2. Time-averaging of pressure in coupling to mass flow rate

Following the preliminary study, i.e., mesh independence and DPM study, the model was run with $\dot{m}$ coupled to A_{sp}. However, in practice, due to the inertia of the melt, the injected melt will not be able to respond to the extreme high frequency changes instantaneously, since A_{sp} is recorded for every timestep, with the timestep size being 5x10^{-8} s. Hence time-averaging is employed to the measured pressure thereby adjusting the mass flow rate as per equation (4). Three different time averaging durations were run to understand the effect of time-averaging on mass flow rate, and they were instantaneous, 5 μs and 50 μs. For the three mentioned runs, an initial mass flow rate of 0.016 kg s^{-1} was considered, and for this nominal mass flow rate, under the static aspiration pressure of 75 kPa, the constant K presented in equation (4) was evaluated to be 3.2 x 10^{-7} kg s^{-1} Pa^{-1}. As the simulation progresses, the aspiration pressure continuously varies, due to the disturbance in the gas flow-field, leading to changes in the mass flow rate, hence for the instantaneous run the aspiration pressure obtained at the monitor (Fig. 3) was updated into the A_{sp}, equation (4) without any time-averaging to calculate the mass flow rate, whereas for time-averaged runs, the aspiration pressure obtained at the monitor (Fig. 3) was 5 μs and 50 μs time-averaged, respectively, before being updated into the A_{sp} term to obtain the mass flow rate value.

The instantaneous, 5 μs time–averaged and 50 μs time–averaged mass flow rate plot obtained via UDF is presented in Fig. 6, and were analysed. For the instantaneous case, an initial rapid fluctuation can be seen at the start of the injection but later smooths out. When the 5 μs time averaging is introduced, a marginal change in the initial mass flow rate is observed, as seen in the Fig. 6, but as time progresses it is evident the overall trend of the 5 μs time–averaged plot follows the same trend of the mass flow rate plot of the instantaneous model. From the above trend it was apparent the applied time-averaging period i.e. 5 μs showed little to no smoothing effect on the oscillation in the melt flow rate. This indicated the time-averaging period should be higher than that of 5 μs. In fact, from the Fig. 6 for most of the plot the blue plot (5 μs time-averaging) exactly overlaps onto the black plot (Instantaneous). For the considered melt injection velocity of 1.38 m s^{-1}, considering the duration of the time-averaging period of 5 μs, the melt displaces about 7 μm, which would not be the same in a physical atomisation as the surface tension and viscosity tends to dampen such small amplitude oscillations. Hence, the time-averaging was increased substantially to 50 μs to make the melt respond to the pressure variations more realistically. In the 50 μs time-averaged mass flow rate plot as seen from the Fig. 6, a more distinct difference is observed, where the trend of the mass flow rate is different to both the instantaneous and the 5 μs mass flow rate plots. In the 50 μs time-averaging plot (Fig. 6) it can be observed that the low frequency is preserved, eliminating only the higher frequencies.
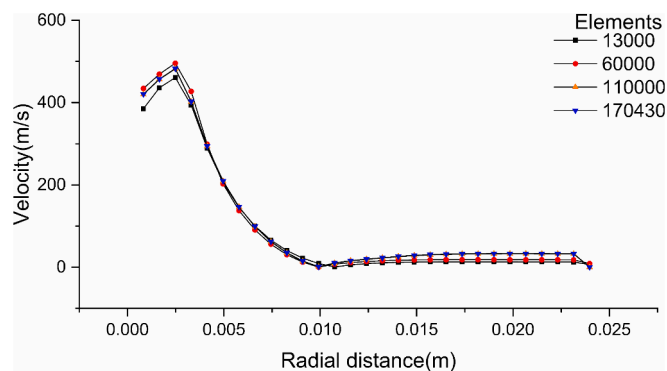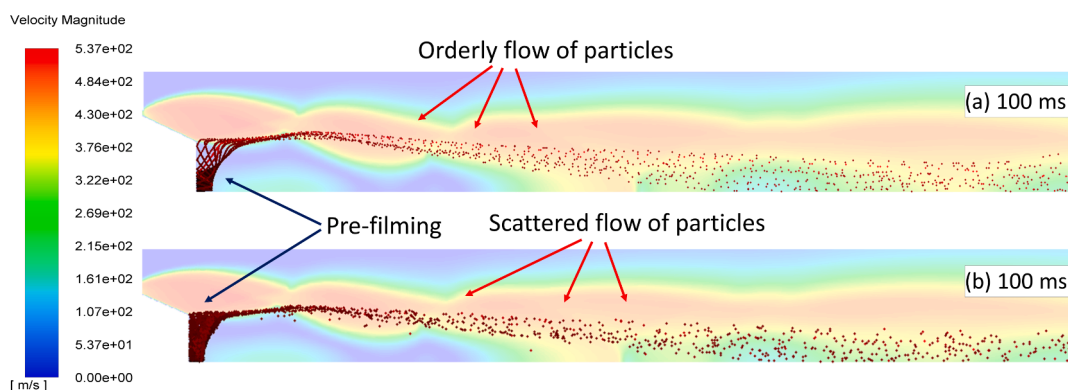
Fig. 5. Particle trajectories with velocity contours of the flow-field in the background are presented; (a) shows the particle trajectories taken at 100 ms without employing stochastic tracking, (b) shows the particle trajectories taken at 100 ms employing stochastic tracking. Both (a) and (b) presents the process of pre-filming (melt touching the melt nozzle tip).
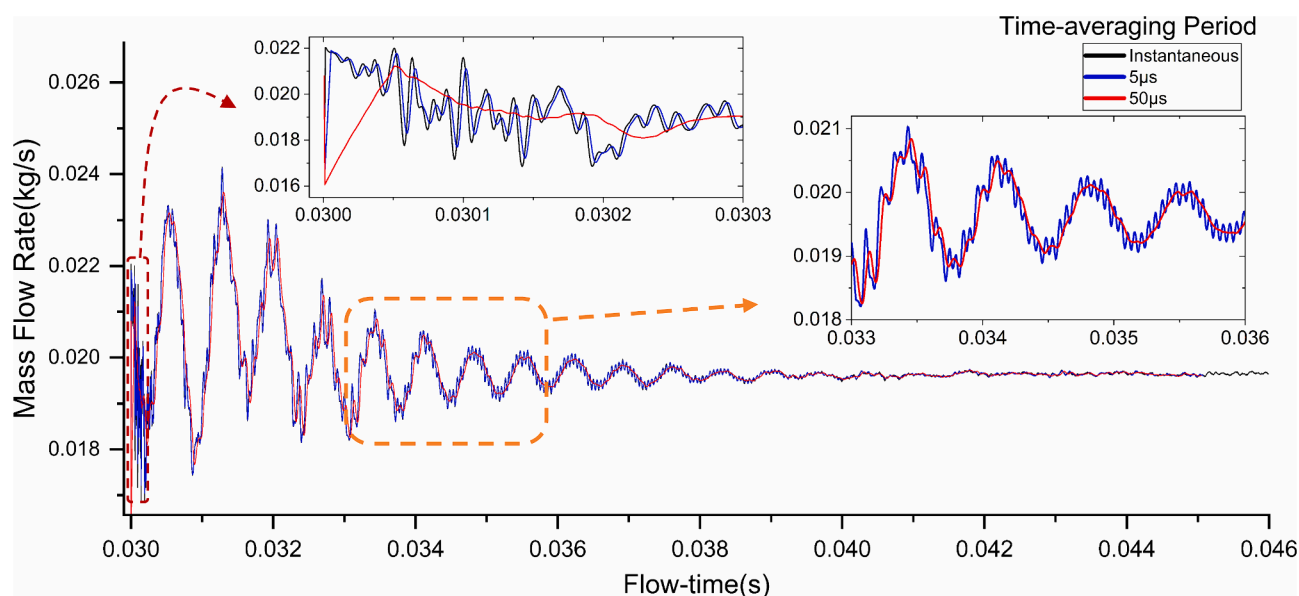

Fig. 6. Injection mass flow rate plots showing the difference in the three time-averaging period – Instantaneous, 5 µs, and 50 µs.

Hence, 50 µs time-averaging is used for the rest of this paper.

The outlined coupled model was run with three nominal mass flow rates as presented in Table 1 1 kg min^{-1} (0.016 kg s^{-1}), 2 kg min^{-1} (0.033 kg s^{-1}) and 4 kg min^{-1} (0.066 kg s^{-1}), having GMR values 5.5, 2.6, and 1.32 respectively. For all three nominal mass flow rates, the inlet gas operates at a constant pressure of 4.5 MPa with a consistent mass flow rate of 0.088 kg s^{-1}. Although the melt mass flow rates (Table 1) employed in this study are generally much lower than those in industrial-scale operations, this model which is based on the research-scale atomiser incorporates realistic GMRs (Table 1) that are applicable to both research and industrial-scales. Even though the nominal flow rate values are applied initially, the actual mass flows adjust according to the A_{sp}. As the A_{sp} fluctuates with time, the mass flow changes in accordance to equation (4). The A_{sp} for all three models is 50 µs time-

averaged, and incorporated into the mass flow rate equation, equation (4). The constant K in equation (4) for the three mass flow rates is 3.2 x 10–7 kg s^{-1} Pa^{-1}, 6.6 x 10^{-7} kg s^{-1} Pa^{-1}, and 1.3 x 10^{-6} kg s^{-1} Pa^{-1} respectively. The time-averaged injected mass flow rate was recorded for every timestep. Also, the mass flow of melt particles leaving through the outlet of the domain was recorded for every timestep, and these were then time-averaged over 50 µs. The results of these mass flow rates are discussed in detail in the results section below.

3. Results

3.1. 1 kg min^{-1} model

The GMR = 5.5 model having a gas and melt flow rate of 0.088 kg s^{-1} and 1 kg min^{-1} (0.016 kg s^{-1}), respectively, was run for 84 ms (30 to 114 ms). The injection mass flow rate plot wherein the mass flow rate is calculated from time-averaged A_{sp} in equation (4), is presented in Fig. 7. The oscillations observed are a result of the varying A_{sp} to which they are coupled. From the zoomed section of the plot shown in Fig. 7 it can be observed that there is an initial steep increase in the mass flow rate value for the first 0.4 ms and thereafter evolves into a damped oscillation. From 30.5 ms series of high amplitude fluctuations are observed before
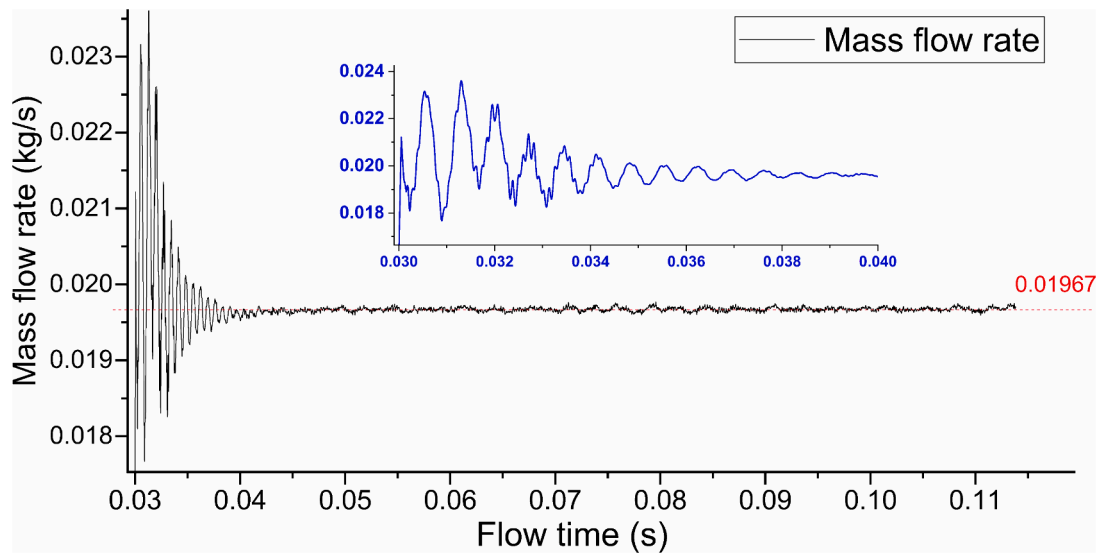
Table 1
Nominal melt flow rates and their respective GMRs used in this study.

Operating Pressure (MPa)	Gas Flow rate (kg s^{-1})	Melt flow rate (kg min^{-1})	Melt Flow rate (kg s^{-1})	GMR
4.5	0.088	1	0.016	5.5
4.5	0.088	2	0.033	2.6
4.5	0.088	4	0.066	1.32

Fig. 7. Injection mass flow rate plot of 1 kg min^{-1} (GMR = 5.5) model, time-averaged over 50 μs.

the fluctuation damps out. It could be observed that within these high amplitude fluctuations there is an overlaid high frequency fluctuation which also damps out eventually at t > 34 ms. This initial fluctuation can be attributed to the onset of the melt injection into the domain which disturbs the gas flow-field because of the change in the aspiration pressure. As time progresses further the oscillations become almost entirely damped out, transitioning into a near-steady mass flow rate for the rest of the simulation having an approximately constant value of 0.01967 $\pm$ 0.00003 kg s^{-1}. This is 18.5 % higher when compared against the nominal mass flow rate (0.0166 kg s^{-1}), indicating that the gas-only flow is not a good indicator of the atomiser performance in two-phase flow. Nevertheless, even without the time-averaging as seen in the Fig. 6 the mass flow rate reaches the same near–constant value indicating that the 1 kg min^{-1} (GMR = 5.5) model quickly become highly stable and not volatile as typically seen in the physical atomisers.

The particle trajectories with the velocity contours of the gas flow-field in the background are presented in Fig. 8. On comparing Fig. 8a with Fig. 8 b a large disturbance can be observed in the flow-field. This disturbance can be attributed to the onset of melt injection into the domain (atomisation chamber) that disrupts the steady gas flow. To understand this, three white dashed guide-lines (i), (ii), and (iii) are pinned at Fig. 8a, at the first Mach-disk, stagnation point, and second Mach-disk, respectively, to compare it against Fig. 8b to show the disturbance that takes place when melt is injected. When compared, it can be seen, all the three mentioned key points shift distinctly in Fig. 8b. Following the melt injection, the melt undergoes pre-filming at around 31.5 ms with its melt pool head building-up almost perpendicular to the direction of the flow-field as shown in Fig. 8c. This wall like melt build-up, by the advancing melt, is due to the opposing force of the recirculation zone. The melt that is pulled radially out by the recirculation zone, when it comes in contact with the supersonic gas jet, is swiftly pushed downstream owing to the kinetic energy possessed by the supersonic flow-field. Until 32 ms it can be observed that the particles pushed downstream from the first shock-cell are tightly collimated (Fig. 8c, d & e), but later as the time progresses the particles start to disperse even from the first shock-cell (Fig. 8f). This transition of particle trajectories from being collimated to much more dispersed later may be attributed to the mass build-up in the domain which can be inferred by comparing the injection mass flow rate plot and the particle out-flow rate plot obtained at the outlet of the domain which is presented in Fig. 9. Due to the mass build-up in the domain, the melt pool head advances 2N$_d$ (nozzle-diameter) downstream until 57 ms, remaining in the same location for the remainder of the simulation. This is shown in

Fig. 8h. The stabilisation of the melt pool head downstream at t > 57 ms is confirmed by comparing the melt pool head taken at 57 ms against 80 ms using the secondary white dashed line shown in Fig. 8h&i.

To identify different frequencies of fluctuation, present in the injected mass flow rate plot, Fast Fourier Transform (FFT) analysis was conducted. From the analysis two distinct frequencies were found: a dominant low frequency and a weaker high frequency, as shown in Fig. 10. The lower frequency was found to be 1.4 kHz (0.71 ms), and the higher frequency was found to be 9.1 kHz (0.1 ms), and the ratio of their power was 49.

From velocity contours of the gas flow-field presented in Fig. 11 it was observed as the melt was injected the gas flow-field was disturbed from its initial steady-state, undergoing flow-field fluctuations, but continued to exist in the closed-wake condition. This initial fluctuation due to the onset of the melt injection is presented in Fig. 11. Even though the melt is present in all the frames of Fig. 11, only the velocity contours are presented to better visualise the gas flow-field. A white guide-line is fixed at the first Mach-disk of Fig. 11a and is compared against the other flow times. It can be seen that the flow-field oscillates by shrinking and expanding i.e. moving upstream and downstream. Moreover, from the velocity contours (Fig. 11b-e), the downstream movement of the melt pool head as seen in Fig. 8e–h is observed and the locations are marked using black circles. The downstream movement of the melt pool head is more evidently seen in Fig. 12. The flow-field after the initial fluctuation (Fig. 11) progressively damps out in its fluctuation while still continuing to exist in closed-wake condition. At 32.2 ms, as the fluctuation continues to damp out, the flow field transitions into open-wake condition, remaining in the same configuration for the remainder of the simulation. Subsequently, at t > 36 ms the flow-field stabilises into a steady-state. This is shown in Fig. 12 by stacking up velocity contours obtained at close consecutive flow times and pinning five guide-lines at key locations of the flow field in the first frame of the stack and comparing them against the other frames. Guide-lines (i), (ii), (iii), (iv), and (v) are pinned at the melt pool head tip, end of first shock-cell, end of second shock-cell, stagnation point, and second Mach-disk, respectively. Guide-line (i) is highlighted in black colour to show the continuous downstream movement of the melt pool head that continues until 57 ms, whereas the others are white in colour to represent they are fixed. The locations of the melt pool head in Fig. 12 are marked using red circles. Comparing the flow-field fluctuation with the melt fluctuation frequencies obtained from the FFT analysis, it was determined that the melt fluctuation of 1.4 kHz corresponds to the initial flow-field fluctuation. However, the melt fluctuation of 9.1 kHz, could not be identified in the
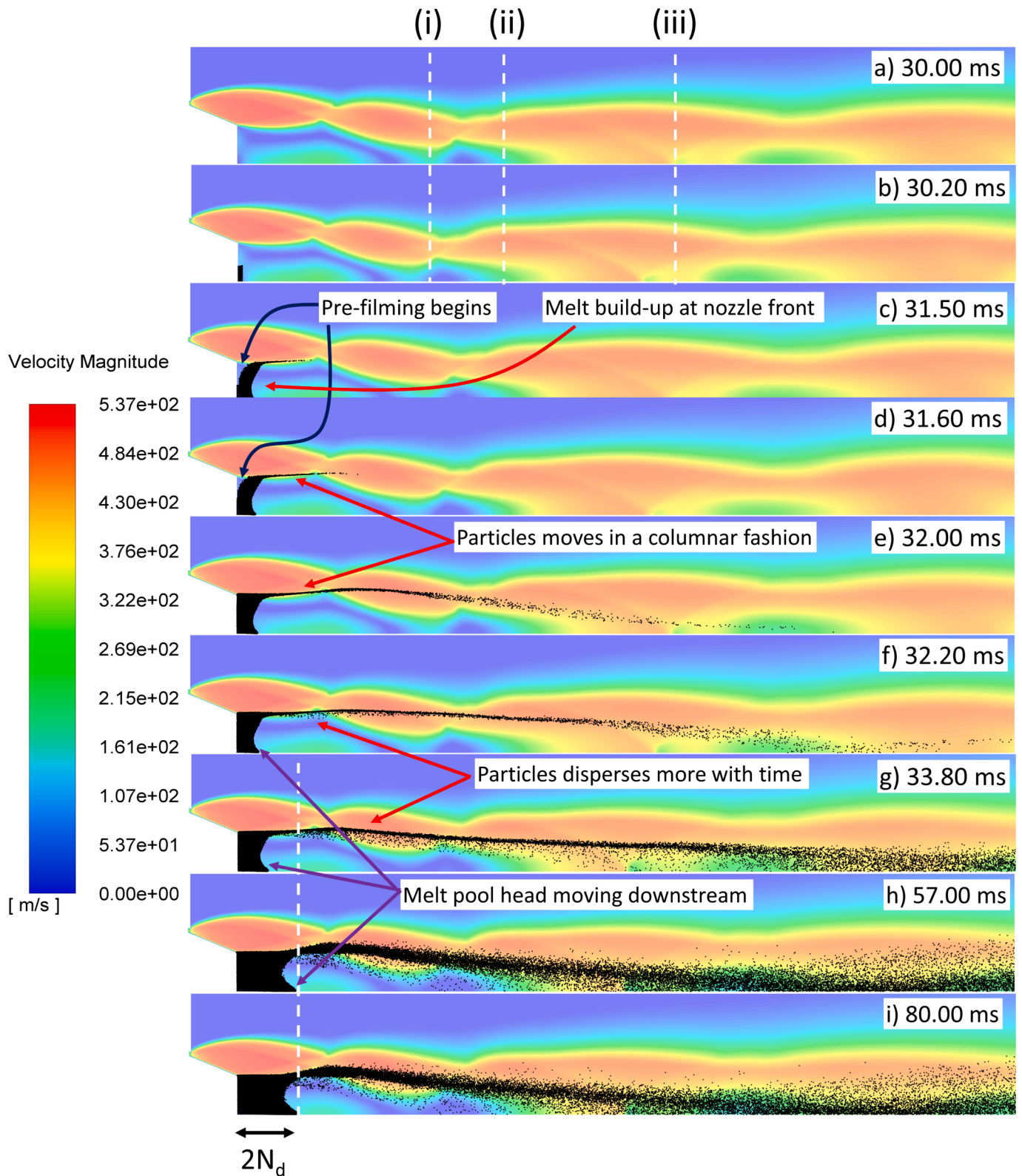
Fig. 8. Particle trajectories with velocity contours in the background are presented for the 1 kg min^{-1} model. At the 57 ms the extent of melt pool head movement stabilises at the distance of $2N_d$ (aspect ratio – 7:1) from the melt nozzle exit. This is established by comparing the melt pool head at 80 ms against 57 ms using the secondary white dashed lines seen in frame h and i.

flow-field.

The gas flow-fields were examined against the local maxima and local minima of the two dominant melt frequencies i.e. 1.4 kHz and 9.1 kHz seen in the injection mass flow rate plot (Fig. 7) obtained via the FFT

analysis, to observe for any significant changes. It was observed, at local minima of the 1.4 kHz fluctuation, the wake region reduced in its size i.e the first Mach-disk moved upstream reducing the area of the wake region. The first Mach-disk is said to be moved upstream or downstream
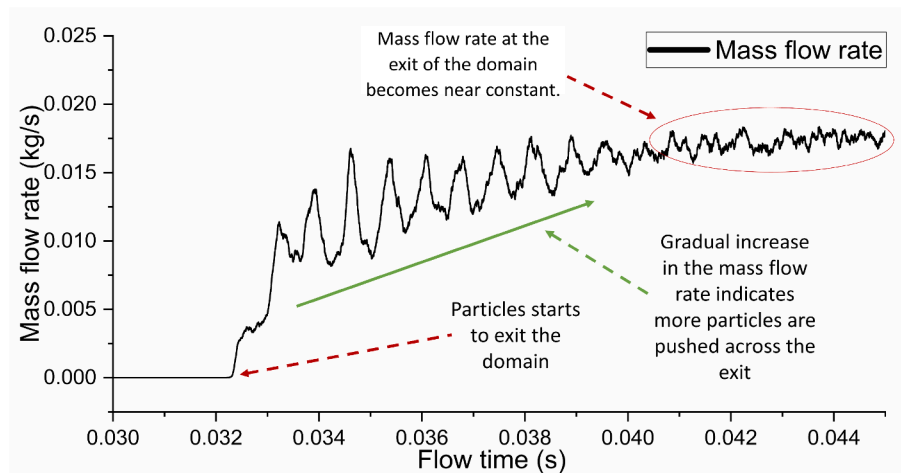
Fig. 9. Mass out-flow rate taken at the outlet (exit) of the domain showing particle takes around 2.4 ms to reach to the outlet.
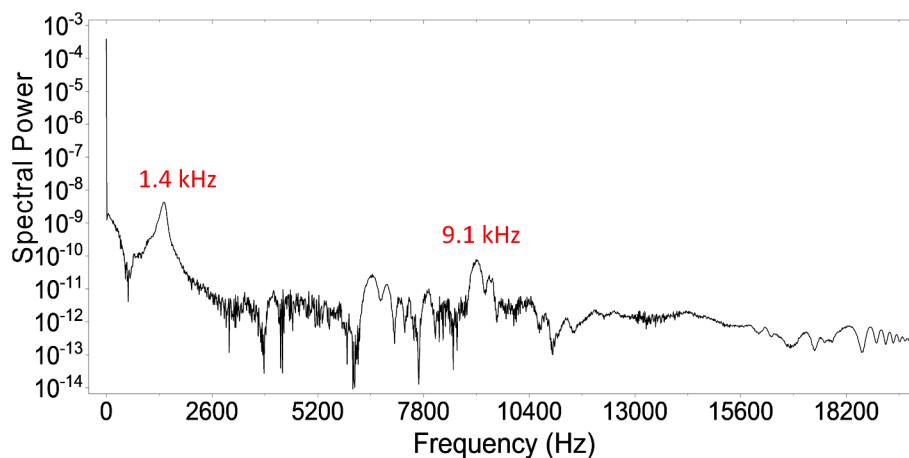

Fig. 10. Fast-Fourier Transform (FFT) of injected mass flow rate showing significant frequencies present in the fluctuation.

when compared against the guide-line (i), presented in Fig. 11a, fixed at first Mach-disk. The flow-field corresponding to the local minima, showing reduced wake region is presented in Fig. 11b&d. Similarly, at local maxima, the first Mach-disk moved downstream, displaying increased area of the wake region, as observed in Fig. 11c&e. However, for the higher frequency, 9.1 kHz, there was no correlation between the changes in the flow-field and the local extrema of the melt fluctuation. Furthermore, despite the significant gas and melt instabilities observed at the onset of the melt injection, the process does not alternate between closed- to open-wake condition. Instead, the instabilities were damped out within a short time, resulting in a steady-state flow for both the gas and the melt. This steady and stable process confirms that the initial mass flow rate of 1 kg min^{-1} (GMR = 5.5) is insufficient to provide a full understanding of the pulsation mechanism present in the atomisation process. Hence, a higher mass flow rate value of 2 kg min^{-1} was run.

3.2. 2 kg min^{-1} model

The GMR = 2.6 model having a gas and melt flow rate of 0.088 kg s^{-1} and 2 kg min^{-1} (0.033 kg s^{-1}), respectively, was run for 74 ms (30 to 104 ms). The injection mass flow rate plot obtained from equation (4) i.e. from the time-averaged A_{sp} with a K corresponding to the nominal $\dot{m}$ = 2 kg min^{-1}, is presented in the Fig. 13. The initial fluctuations that can be observed seen in Fig. 7 for the 1 kg min^{-1} model can also be seen in Fig. 13, almost replicating the initial trend of the plot. There is also the presence of overlapped frequency in the plot. From FFT analysis of the

melt fluctuation seen in Fig. 13, a lower frequency of 1.4 kHz, a mid-frequency of 9 kHz and a higher frequency of the 19.7 kHz, was obtained — presented in Fig. 14. After the initial fluctuation, at 39 ms, even though there isn't any significant pulsation as in previous cycles (Fig. 13), there is a gradual rise in the injected mass flow rate until it reaches its peak at 49 ms subsequently followed by a gradual fall. At t > 66.5 ms, the mass flow rate stabilises into a steady-state, at a value of 0.04032 ± 0.00008 kg s^{-1}, which is 21.5 % higher than the nominal mass flow rate.

The pattern of flow distribution of particles in the 2 kg min^{-1} model is similar to that of the 1 kg min^{-1} model. With the onset of the melt injection a large disturbance is observed in the gas flow–field. Following the injection, the particles undergo pre–filming, by touching the melt nozzle tip at 31.8 ms. The figure for the pre-filming is not presented as the particles' trajectories were same as seen in Fig. 8c&d. However, unlike the 1 kg min^{-1} model, due to the increased mass loading in the domain, the melt pool head continued to move further downstream before stabilising at $4N_d$ downstream at t > 70 ms. This is shown in Fig. 15c, where a white guide-line is fixed at the melt pool head at t = 70 ms to compare its movement against the others, illustrating the downstream movement of the melt pool head. Moreover, due to the increased mass loading in the domain, there is an increased particle dispersion. Also, it is evident the melt pool head morphologically changes over time by becoming more pointed as shown in the Fig. 15.

On observing the flow-field contours, initial fluctuation during the onset of melt injection seen in the 2 kg min^{-1} case was the same as the
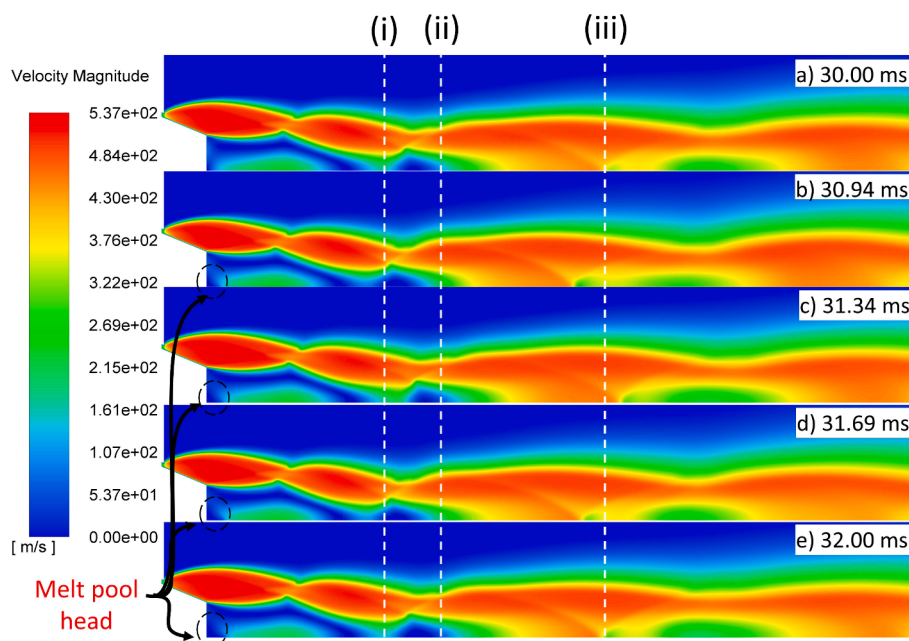
Fig. 11. Velocity contours showing flow-field fluctuation during the onset of the melt injection without the particles for the 1 kg min^{-1} model. The melt pool heads of the frames, b–e, are marked in the black circle. A guide-line is pinned at the first Mach-disk of frame (a) and is compared against the rest of the frames to show the to-and-fro movement of the flow-field fluctuation.
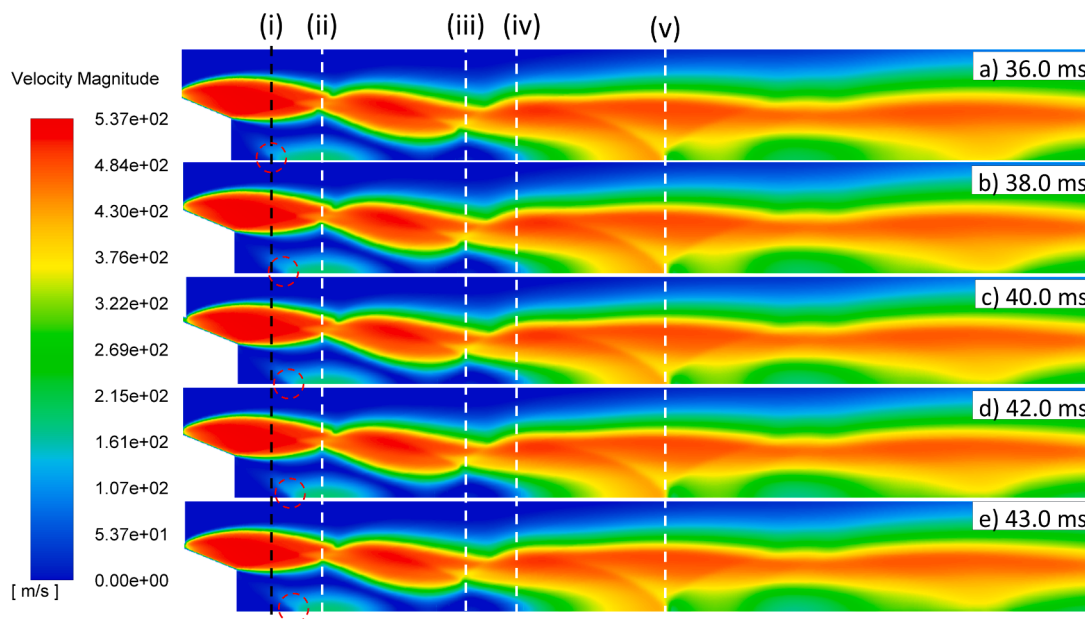

Fig. 12. All the velocity contours of 1 kg min^{-1} for different flow time are presented in sequential order indicating the flow-field exist in open-wake condition and in steady-state from t > 36 ms. The melt pool heads of the all the frames are marked in red circles.

one seen in the 1 kg min^{-1} case. The flow-field fluctuated by displacing upstream and downstream until 32.5 as seen in Fig. 11 of 1 kg min^{-1} case, and subsequently after 32.5 ms the flow-field transitioned into open-wake condition. Even though the flow-field continued to exist in open-wake condition, it continued to fluctuate. However, the fluctuation gradually reduced in its spatial oscillation, converging into a steady-state flow around 40 ms, still continuing to exist under open-wake condition as presented in Fig. 16. It is notable that the steady-state flow condition existed only for a brief period of time from 40 to 60 ms, as shown in the Fig. 16b&c. This is illustrated by pinning four guide-lines at 40 ms i.e. Fig. 16b and is compared against Fig. 16c (t = 60 ms).

Guide-lines (i), (ii), (iii), and (iv) were pinned at melt pool head tip, end of second shock-cell, stagnation point, and second Mach-disk, respectively. It can observed that in Fig. 16b and Fig. 16c, apart from melt pool head moving downstream, the flow-field exists in steady-state. Around 60 ms there was an onset of a fluctuation in the flow-field, which started gradually but with time grew in its spatial magnitude and continued to persist for the remainder of the simulation. As the fluctuation continued to grow spatially, at t = 65 ms the wake transitioned from being open-wake to alternating wake i.e. from open- to closed-wake condition, and thereafter displayed continuous alternation in its wake for the remainder of the simulation. This transition in the flow-field fluctuation
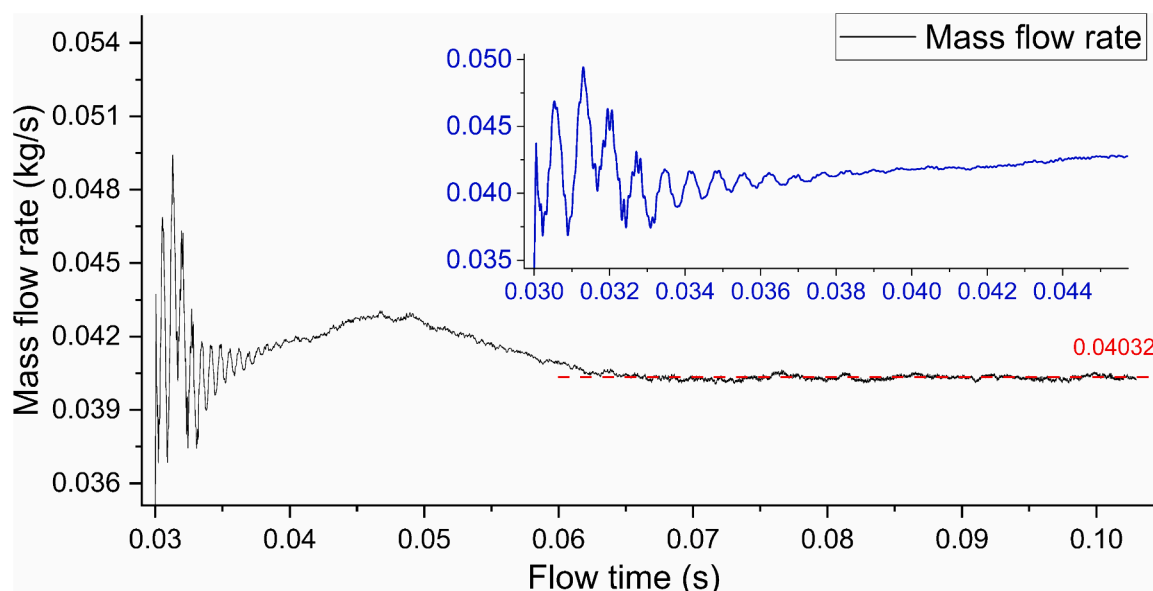
Fig. 13. Injection mass flow rate of 2 kg min^{-1} model, showing initial fluctuation followed by a gradual rise and fall trend, and subsequently becoming near steady-state at 66.5 ms having a mass flow rate of 0.04032 kg s^{-1}, shown by the red horizontal dashed lines.
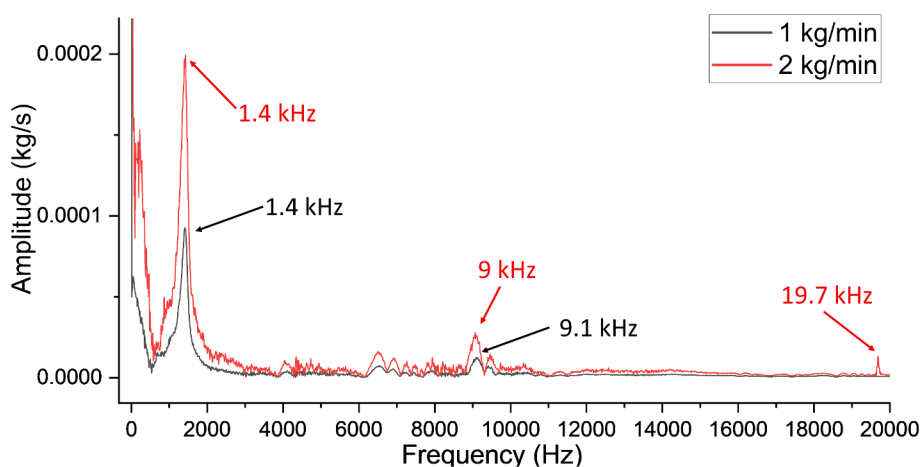

Fig. 14. FFT plot of 1 & 2 kg min^{-1} models showing their corresponding dominant frequencies. The former possess two dominant frequencies, while the latter possess three.

shifting from open-wake fluctuation to alternating wake fluctuation is presented in Fig. 17. Two guide-lines (i) and (ii) are pinned in the Fig. 17a, at the end of the first and second shock-cell, respectively, and were compared against the rest of the frames. The fluctuation undergoing in open-wake condition is seen in Fig. 17a-d and the fluctuation in alternating wake condition seen at t > 65 ms is observed in Fig. 17e-h. Moreover, the transitional fluctuation demonstrates the progressive spatial growth of the flow-field which is evident when comparing the size of the second shock-cell in Fig. 17c against that in Fig. 17g. However, the first shock-cell remains fixed in its spatial extent throughout the transitional fluctuation as observed through guide-line (i). The fluctuation attained its maximum spatial oscillation around 70 ms, and hence series of velocity contours were recorded at close time periods at 70 ms, to understand the phenomena. The contour stacks are shown in Fig. 18, where guide–lines are pinned at key locations to analyse the movement of the flow–field features during fluctuation. Vertical white guide-lines (i) and (ii) are pinned in the Fig. 18a, at end of the first shock-cell and at the first Mach-disk, respectively. Similarly, another secondary guide-line is used to trace the end of the second shock-cell throughout the fluctuation. From Fig. 18 it is evident that during flow-

field fluctuations, the first shock-cell remains fixed and unchanged in its spatial extent, whereas the second shock-cell undergoes fluctuation by changing its spatial extent. This is seen through the secondary white dashed guide-lines, where the line traced the expanding and contracting end of the shock-cell; Fig. 18a-f, and Fig. 18g-k, respectively. Through the help of guide-line (ii) it can be confirmed, that the flow-field undergoes a repeated and orderly fluctuation, with the flow–field alternating between open-to closed wake condition. The first Mach-disk which is seen in the Fig. 18a, which indicates that the flow-field exists in closed-wake condition, gradually transitioned to open-wake condition, i.e., without the presence of any significant Mach-disk (Fig. 18f), and returned back to its original configuration of closed-wake condition having the same configuration as Fig. 18a in Fig. 18k. In addition to the above-mentioned observations, a wave propagating from the second Mach-disk and continuing to propagate until the end of domain, was also observed. This observed wave propagation is marked by the blue ellipses in Fig. 18. The flow-field fluctuation at t > 60 ms was evaluated for its frequency and was found to be 20 kHz. The mass flow rate plot was examined to check for frequency corresponding to the frequency of flow-field fluctuation. The high frequency melt fluctuation, 19.7 kHz,
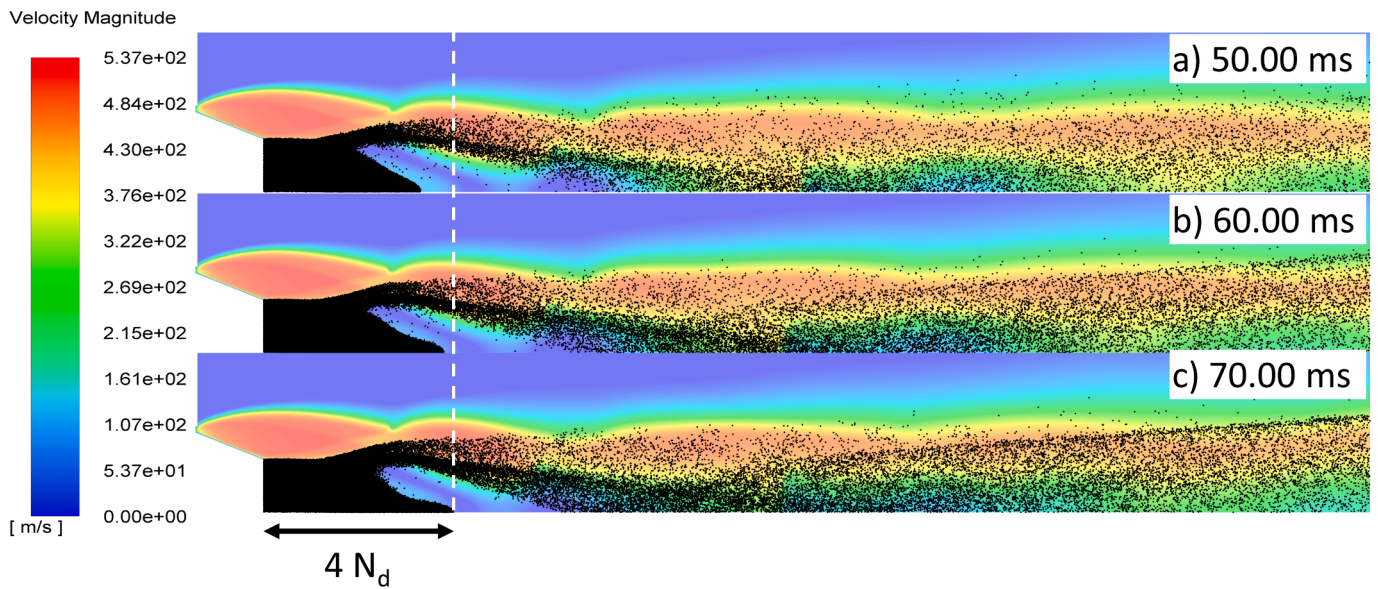
Velocity Magnitude

Fig. 15. Particle trajectories of the 2 kg min^{-1} model with the velocity contour in the background showing melt pool head movement downstream as well as the dispersal of the particles. The particles trajectories stabilise at $4N_d$ (aspect ratio – 7:1) at t > 70 ms.
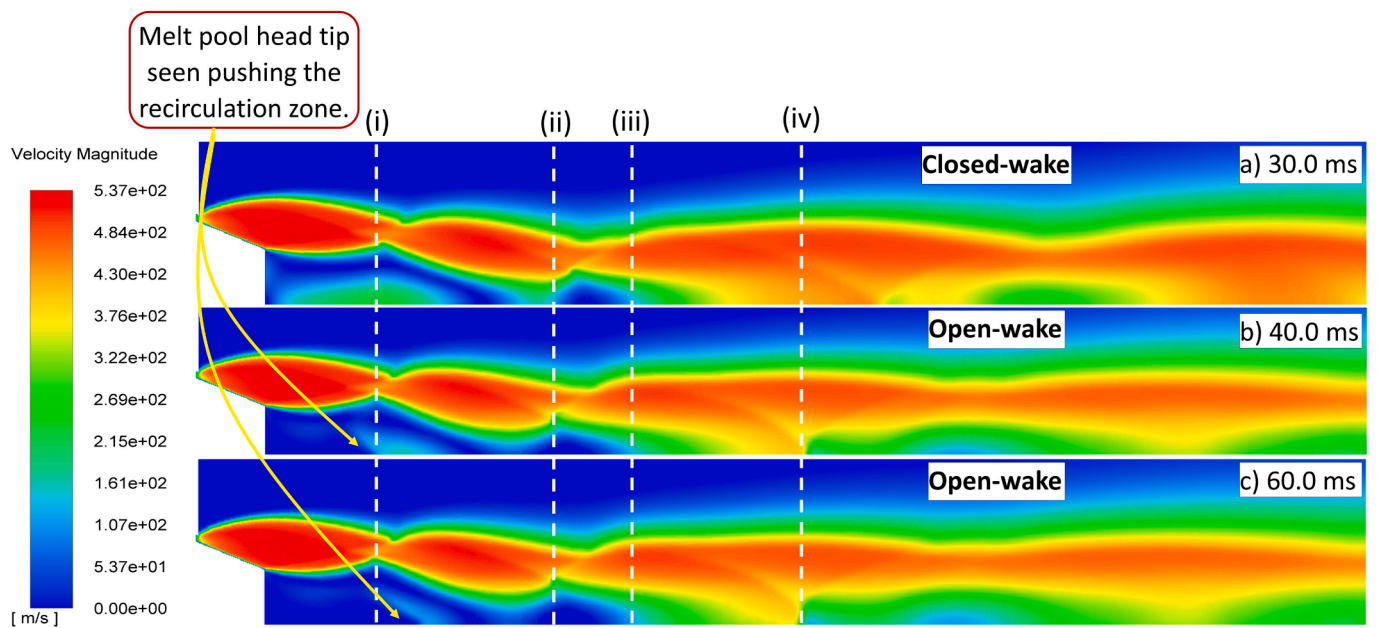

Fig. 16. Velocity coutours of the flow-field of 2 kg min^{-1} case stacked up at different flow times. At 40 ms (frame b), four guide-lines namely (i), (ii), (iii), & (iv) are pinned at melt pool head tip, end of second shock-cell, stagnation point, and second Mach-disk, respectively, to compare against the rest of the stacks, to illustrate the changes in the gas flow-field. This shows the flow-field at t > 40 ms exists in open-wake condition. Melt pool head continues to move downstream beyond 40 ms, but stabilises at 70 ms.

obtained from the FFT analysis having a negligible amplitude (Fig. 14) corresponded to this flow-field fluctuation. The reason for the difference in the flow-field fluctuation frequency (20 kHz) and the mass flow rate high-frequency fluctuation (19.7 kHz) is due to the lack of additional significant figures in the recorded flow times, leading to the difference of 300 Hz. In addition to this, the flow-field fluctuations were examined against the local extrema of the frequencies obtained from the FFT analysis (Fig. 14) i.e. 1.4 Hz, 9 kHz, and 19.7 Hz, to observe for any alternation in the wake condition. The flow-field fluctuation seen during the onset of the melt injection as seen in Fig. 11 corresponded to the low frequency, 1.4 kHz. However, the local extrema of this frequency did not correspond to an alternating wake condition. Similarly, no correlation

could be observed from the flow-field fluctuation for the mid-frequency fluctuation of 9 kHz. It was interesting to find, when the high frequency fluctuation of 19.7 kHz was examined, the flow-field fluctuation having frequency of 20 kHz displayed profound alternation in the wake condition, but on examining the mass flow rate plot, starting from the onset of this high frequency fluctuation i.e. t > 60 ms no significant change in the amplitude could be observed. However, on further examining a high frequency fluctuation having negligible amplitude of the order 8x10^{-5} kg s^{-1} i.e. smaller than the average mass flow rate by a factor of ∼ 500, was found.

With a GMR value of 2.6, the 2 kg min^{-1} case is pronounced as a gas dominant process to a certain degree if not as the 1 kg min^{-1} case. The
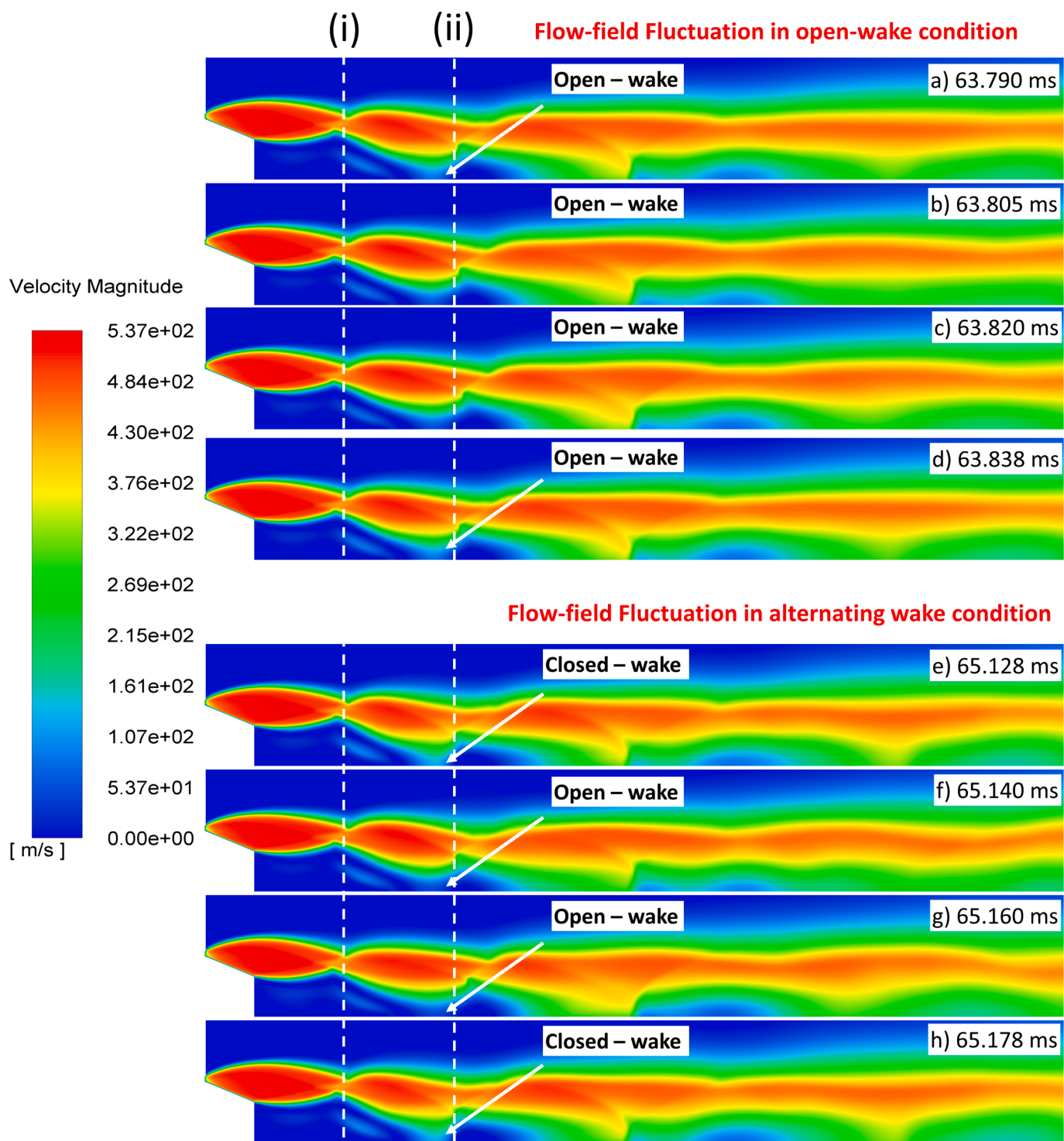
Fig. 17. Velocity contours of the flow-field fluctuation of 2 kg min^{-1} case showing the transition from open-wake fluctuation to alternating wake fluctuation. Frame a-d shows the flow-field undergoing fluctuation in open-wake condition. Frame e-f shows the flow-field undergoing alternating wake fluctuation. The progressive growth in the flow-field fluctuation between the two fluctuations is observed by comparing the second shock-cells of frame c and g.

process exhibited continuous flow-field fluctuation, however no significant melt instability could be observed. Hence a higher mass flow rate of 4 kg min^{-1} (0.066 kg s^{-1}) having a GMR value of 1.32, close to that of industrial standards (GMR ≈ 1) was considered to further examine the gas–melt interactions.

3.3. 4 kg min^{-1} model

The GMR = 1.32 model having a gas and melt flow rate of 0.088 kg s^{-1} and 4 kg min^{-1} (0.066 kg s^{-1}), respectively, was run for 144 ms (30 to 174 ms). Fig. 19 shows the injection mass flow rate plot with zoomed-in section of the initial fluctuation and high frequency fluctuation shown in blue and red, respectively. The injection mass flow rate presented here is obtained through equation (4) wherein the A_{sp} is time-averaged
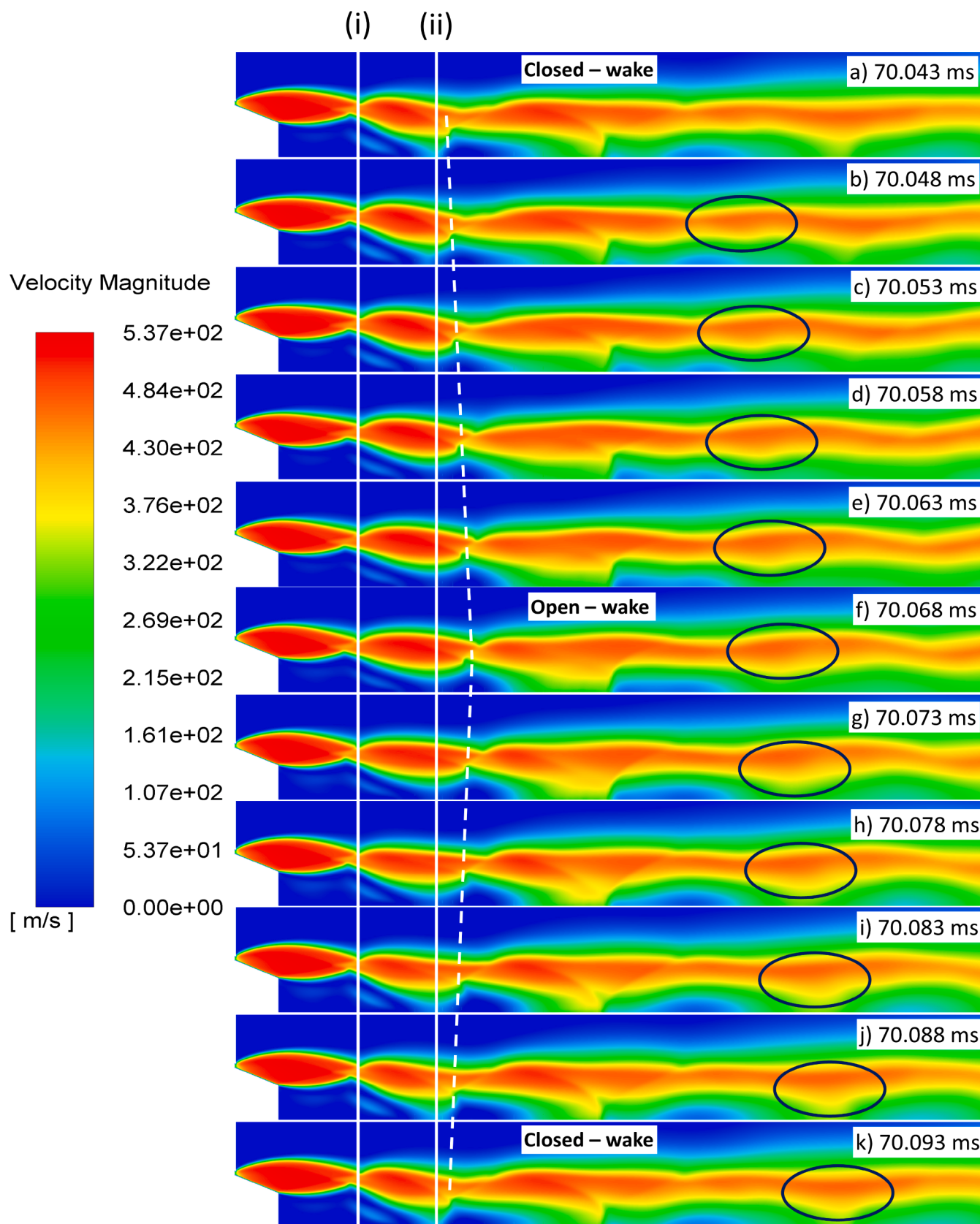
Fig. 18. Velocity contours of the 2 kg min^{-1} model showing a cycle of the repeated alternating flow-field fluctuation. The flow-field transitions from closed-wake condition (frame a) to open-wake (frame f), and subsequently returns to closed-wake (frame k). Two primary guide-lines (i) and (ii) are fixed at the end of the first shock-cell and at the first Mach-disk, respectively, and are used to compare the extent of the flow-field fluctuation against the rest of the frames. Another white dashed line is used to trace the movement of the end of the second shock-cell during the fluctuation. It is seen the first shock-cell did not undergo any change in its shape or length whereas the second shock-cell, as marked with the white dashed line, undergoes changes in its spatial dimensions.
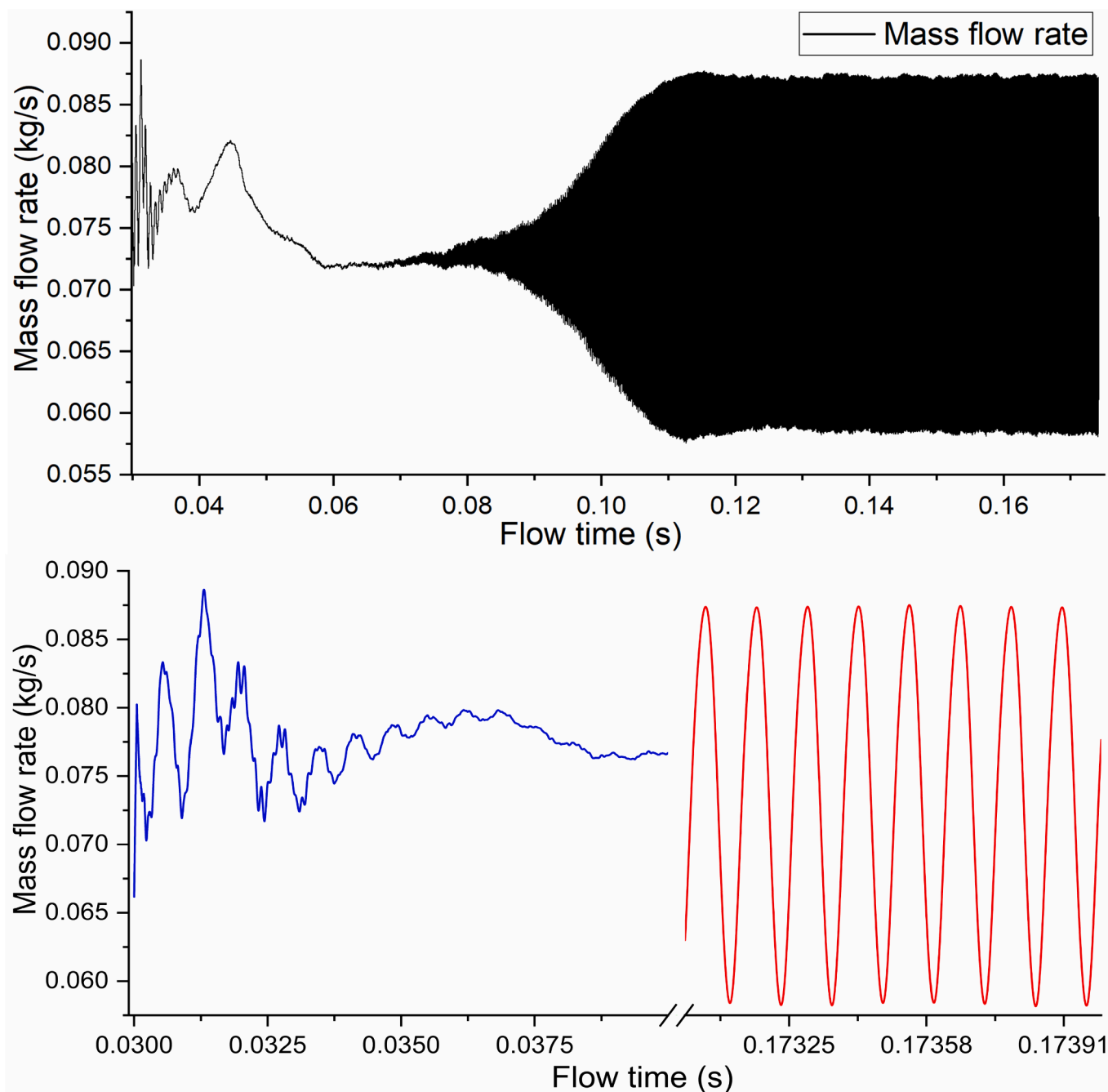
Fig. 19. Injection mass flow rate plot of 4 kg min^{-1} case showing initial fluctuation and the high frequency fluctuation. At t > 60 ms there is an onset of a higher frequency fluctuation that gradually increases in its amplitude and remains constant from t > 110 ms. The zoomed section of the initial fluctuation and the regular repeated fluctuation is also presented.

and the constant K is calculated based on the nominal mass flow rate of 4 kg min^{-1}. The initial fluctuation until 33 ms, due to the onset of melt injection, is very similar to the 1 & 2 kg min^{-1} cases. Subsequently the fluctuations progressively damp out, but an overall increase in the mass flow rate is observed with the fluctuations continuing to damp out. This is seen in Fig. 19, between 33 and 37 ms. Following this the mass flow rate drops until 39 ms and continues to attenuate in its fluctuation in subsequent cycles. From Fig. 19 it can be observed that between 39 and 60 ms there is another rise and fall in the mass flow rate, however, no significant melt fluctuation cycles could be noted. At t > 60 ms an onset of a higher frequency fluctuation is observed that exists for the rest of the simulation time. The high frequency fluctuation gradually increases in amplitude, reaching a maximum amplitude at 110 ms, and subsequently

maintained that peak amplitude for the remainder of the simulation. From the FFT analysis (figure of the result not presented) three frequencies: low frequency of 1.4 kHz, mid frequency of 8.1 kHz, and high frequency of 16.3 kHz were found; out of which only low and mid frequencies were significantly seen in the injection mass flow rate. The fluctuation seen at t > 60 ms corresponds to the mid frequency, 8.1 kHz. The GMR of this fluctuation was evaluated to be 1–1.52.

The particles' trajectories of the 4 kg min^{-1} case is very similar to that of the 1 & 2 kg min^{-1} cases for the first few ms i.e. the same trend in particles evolvement as seen in Fig. 8, except for the time delay in the pre-filming of the melt. The melt undergoes pre-filming at 32.5 ms. In the 1 & 2 kg min^{-1} cases, as seen from Fig. 8c&d, the pre-filming starts by melt that is close to the atomiser axis coming in contact with the melt

15

nozzle tip followed by the melt present radially outward, and gradually extending towards the circumferential edge of the melt nozzle. However, in 4 kg min^{-1} case, the opposite is seen; pre-filming starts with melt present near to the circumferential edge of the melt nozzle coming in contact with the melt nozzle tip, and gradually extending towards melt nozzle centre i.e. atomiser axis. This is shown in Fig. 20a&b. Nevertheless, in all the cases, the particles after being injected, gets pulled radially outwards due to the recirculation zone, subsequently undergoes pre-filming before travelling downstream. Due to the increased mass loading the melt pool head continuously moves downstream, in the same way as illustrated in Fig. 15. Owing to this continuous movement

of the melt pool head, at 47 ms it joins with the particles that were transported downstream by the supersonic gas jet as shown in the Fig. 20d. Due to its continued downstream movement, the melt pool head plunges into the second Mach-disk (Fig. 20e) and continues to move downstream along the axis of the atomiser, becoming denser with particles over time (Fig. 20e-h). Further to this, flares containing particles in groups of small number were propelled downstream at t > 90 ms. This is marked in Fig. 20g&h using red ellipses.

To observe the changes in the gas flow-field the velocity contours were examined. Even though in all three cases, both gas and melt simultaneously exist and interact, to have a better understanding of the
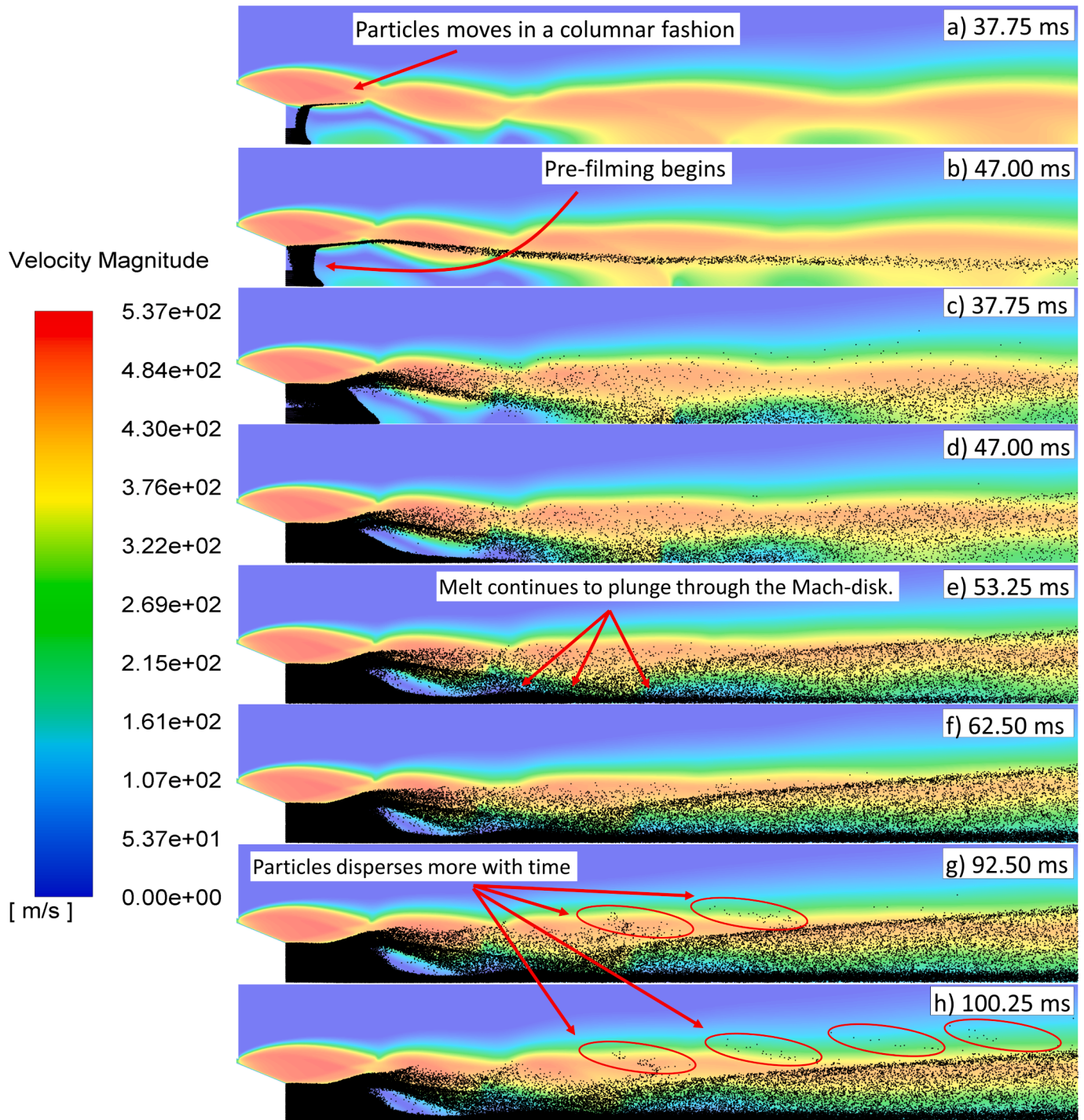

Fig. 20. Particles trajectories of 4 kg min^{-1} model with velocity contour in the background showing increasing dispersion of particles with time; melt pool head plunging through the second Mach-disk (frame e); and particles being propelled downstream in small groups (flares), marked by the red ellipses (frame g & h).

flow of gas, and the changes that happen at and near wake region, only the velocity contours are examined. As reported, with the onset of the melt injection, the gas flow-field is disturbed from its steady-state and undergoes fluctuation. This observed fluctuation lasts until 32 ms and was same as that of the fluctuation seen in Fig. 11 of the 1 kg min⁻¹ i.e. undergoing fluctuation but existing in closed-wake condition. From 32 to 40 ms the flow-field existed in open-wake condition as observed in Fig. 12 while undergoing damped spatial oscillations. As the flow time progressed towards 40 ms the flow-field exhibited further damped spatial oscillations, gradually transitioning towards becoming closed-wake. It subsequently entered into closed-wake condition at 40 ms and simultaneously becoming a steady flow. Shortly thereafter, at 45 ms, the flow-field transitioned into an open-wake condition, and from 50 ms an onset of continuous flow-field fluctuations is observed. The spatial oscillation of the flow-field fluctuations started out gradually along the radial direction and intensified over time, achieving its peak at 55 ms, while still existing in open-wake condition. Velocity contours of the flow-field were obtained at 65 ms, and were stacked sequentially to illustrate the nature of the fluctuation. This is shown in Fig. 21.

Three guide-lines, (i), (ii), and (iii), were pinned in Fig. 21a at the ends of the first, second, and third shock-cell, respectively, and were compared against the rest of the frames in the stack. It can be observed that the spatial extents of the first shock-cell did not change, while those of the second and third shock-cells changed marginally. From Fig. 21 it can be observed, the flow-field did not alternate in its wake condition, and remained in open-wake condition throughout, yet displayed significant fluctuations which were regular in nature. In a cycle of this fluctuation, initially, the lower sonic boundary of the second shock-cell lied in close proximity to the atomiser's axis, marked by the yellow lines (Fig. 21a), and as the fluctuation progressed, the sonic boundary gradually receded away from the atomiser's axis, shown using the curved red line (Fig. 21c). Subsequently, in Fig. 21e the sonic boundary returned back to the same configuration as seen in Fig. 21a. Also, in Fig. 21, a wave propagation was observed starting from the third shock-cell and continuing to propagate until the end of the domain, indicated by the ellipses. The frequency of this regular fluctuation was evaluated to be 20 kHz.

The fluctuation seen in Fig. 21 having the form of a transverse wave, transforms into a fluctuation having spatial oscillations along the axial direction around 85 ms and continuous to grow with time. At 87 ms velocity contours of the transitional flow-field fluctuation is obtained and are stacked sequentially. This is presented in Fig. 22. Two guide-lines (i) and (ii) are pinned at Fig. 22a, at the ends of the first and second shock-cell, respectively. It is evident by comparing the second shock-cells of Fig. 21 against Fig. 22 that the fluctuation undergoes progressive transition towards axial fluctuation. However, the first shock-cell remains fixed in its spatial extent. Two wave propagation from the end of the third shock-cell is observed. This is due to the coexistence of both radial and axial form of fluctuation, resulting in wave propagations as observed in Fig. 22a&c, respectively. The fluctuation grows with time, achieving its maximum spatial oscillation at 100 ms, hence a series of velocity contours were obtained at close consecutive flow times and were stacked sequentially to help understand the fluctuation. This is presented in Fig. 23. Two vertical guide-lines (i) and (ii) were pinned at Fig. 23a, at the end of the first and second shock-cells, respectively. Another two sets of guide-lines were used to trace the extent of movement of the first and second shock-cells of all the frames. It was observed that the second shock-cell underwent a significantly larger fluctuation i.e. change in the shock-cell's spatial dimension along the axial direction, compared to the first shock-cell. During the fluctuation it was evident through the vertical guide-lines, (i) and (ii), that the closed-wake condition, seen in the Fig. 23a, indicated using the first Mach-disk, gradually transitioned into open-wake condition (Fig. 23f), and returned back to its original configuration i.e. closed-wake condition(Fig. 23k). It was observed during the fluctuation, that the same wave propagation pattern starting from the third shock-cell seen in the transverse type fluctuation (Fig. 21) was also seen in Fig. 23. The frequency of this flow-field fluctuation was evaluated to be 8.3 kHz. Corelation between the flow-field fluctuation alternating between open- to closed-wake condition seen in Fig. 23 and the melt pulsation seen in injection mass flow rate plot presented in Fig. 19 were examined. It was found that the mass flow rate fluctuation, 8.1 kHz, obtained from FFT analysis, corresponded to the flow-field fluctuation (8.3 kHz) presented in Fig. 23. Also, efforts were taken to find any observable corelations in
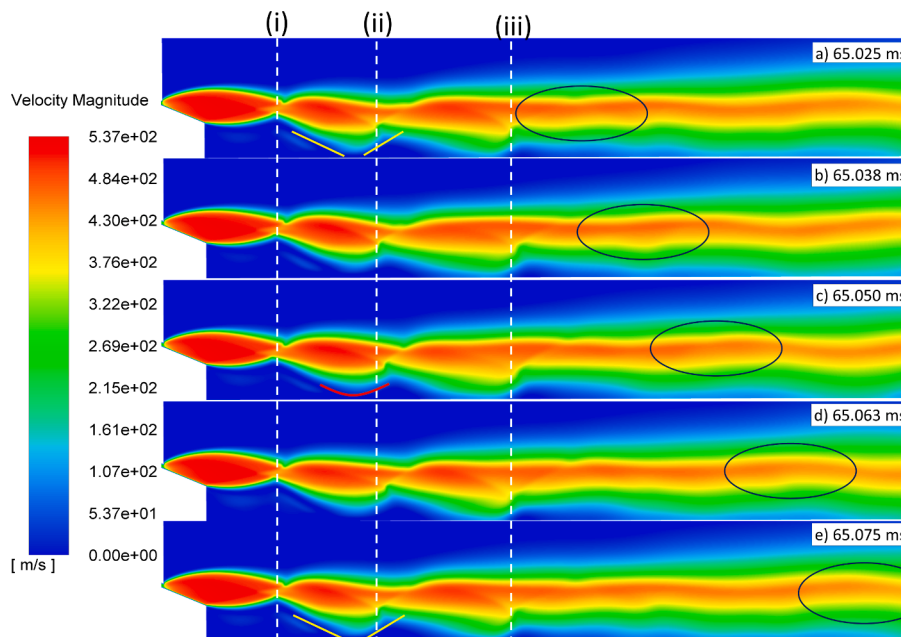

Fig. 21. Velocity contours of the 4 kg min⁻¹ model showing a cycle of the continuous flow-field fluctuation. Three guide-lines (i), (ii), and (iii) are fixed at frame a, at the ends of the first, second and third shock-cell, respectively. The lower sonic boundary of the second shock-cell of frames a & e lies close to the atomiser's axis, as marked by the yellow lines, whereas the sonic boundary seen in frame c is far from the axis, shown using the curved red line. A wave propagation from the second Mach-disk is observed which is marked using blue ellipses. The frequency of the fluctuation was evaluated to be 20 kHz.
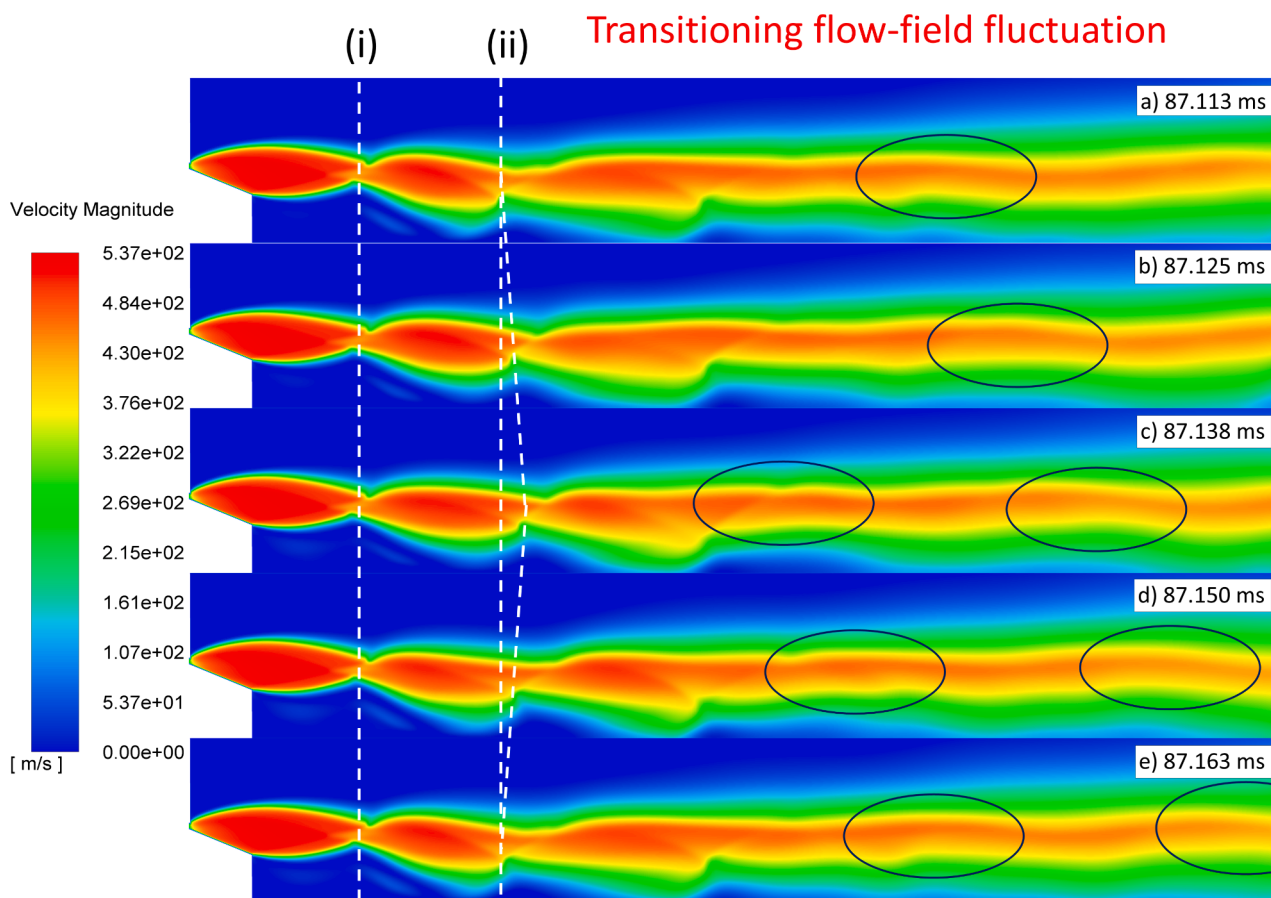
Fig. 22. Velocity contours of the 4 kg min^{-1} case showing the transitional flow-field fluctuation from transverse form fluctuation to axial form of fluctuation. Two guide-lines (i), and (ii) were pinned in the frame a at the end of the first and second shock-cell, respectively. On going transition can be observed in the second shock-cell, undergoing axial fluctuation, whereas the first shock-cell remains fixed. Two wave propagation observed due to the coexistence of radial and axial fluctuation.

the flow-field for the high order flow-field fluctuation of 20 kHz seen in Fig. 21 but no correlation could be drawn from the mass flow rate fluctuation obtained from the FFT analysis.

In addition to this, the flow-field fluctuations were examined for alternating wake condition against the local extrema of the frequencies obtained from the FFT analysis (Fig. 14) i.e. 1.4 kHz, 8.1 kHz, and 16.3 kHz. The initial flow-field fluctuation seen during the onset of the melt injection as seen in Fig. 11 corresponded to the low frequency, 1.4 kHz, however on inspecting the flow-field corresponding to the local extrema, this frequency did not correlate to an alternating wake condition. On inspecting the high frequency melt fluctuation, 16.3 kHz, no correlation could be observed for the flow-field fluctuation. It was interesting to find, when the mid-frequency melt fluctuation of 8.1 kHz was examined, the corresponding flow-field fluctuation having frequency of 8.3 kHz displayed profound alternation in the wake condition. At local minima of the melt fluctuation i.e. low mass flow, the flow-field corresponded to a closed-wake condition (Fig. 23a&k), and at local maxima of the melt fluctuation i.e. high mass flow, the flow-field corresponded to an open-wake condition (Fig. 23f).

4. Discussion

From the above three models, GMR – 5.5 (1 kg min^{-1}), GMR – 2.6 (2 kg min^{-1}) and GMR – 1.32 (4 kg min^{-1}), it is clear that the existence of a significant melt and gas-flow fluctuation due to the gas–melt interactions is not observed for all operating mass flow rates, rather it is seen only in higher mass flow rate values. In the 1 kg min^{-1} model, the melt and the flow-field fluctuations were attenuated by the strong supersonic flow-field that controls and subsides any disturbances caused to

the flow–field due to the melt injection. In the above said model the melt fluctuations seem to subside by 9 ms into the injection of the melt, which indicates the threshold mass loading required to continuously disturb the flow-field is much higher than the mass loading contributed by 1 kg min^{-1}. With a higher mass flow rate melt being injected i.e. 2 kg min^{-1}, it is observed that the fluctuation in the melt attenuates over time to reach a near steady-state similar to the 1 kg min^{-1} case. However, unlike the 1 kg min^{-1} case, due to the increased mass in-flow the melt causes a continuous flow-field fluctuation from t > 65 ms. Nevertheless, the reason for absence of such sustained flow-field fluctuation at 39 < t < 65 ms is uncertain. It appears that, in 2 and 4 kg min^{-1} model, the existence of three levels of frequency namely, low, mid and high frequency were present, whereas in the 1 kg min^{-1} model, only two levels of frequency were present: low and high frequency (Fig. 14). This was confirmed using FFT analysis (Fig. 14) where, even though the mass flow rate plots in the 1 & 2 kg min^{-1} looked similar at t > 41 and t > 39 ms, respectively, there was no significant third frequency observed in the 1 kg min^{-1} model. The initial fluctuations in the injection mass flow rate plot (Fig. 7) seen during the onset of melt injection in the 1 kg min^{-1} model were reflected onto their flow-field fluctuations. However, due to the inadequate mass loading, those fluctuations do not contribute to an extended and continuous fluctuations as seen in the actual physical atomisation process. In the 2 kg min^{-1} model, though the high frequency fluctuation in the mass flow rate was observed to possess a negligible magnitude, only the impact of this frequency can be seen profoundly on the flow-field, and it is this frequency that gives rise to the alternating wake condition, i.e, open- to closed-wake condition. When increasing the mass flow rate to 4 kg min^{-1}, the wake alternation seen in the 2 kg min^{-1} case at 19.7 kHz (Fig. 18), could be seen at 8.1 kHz (Fig. 23),
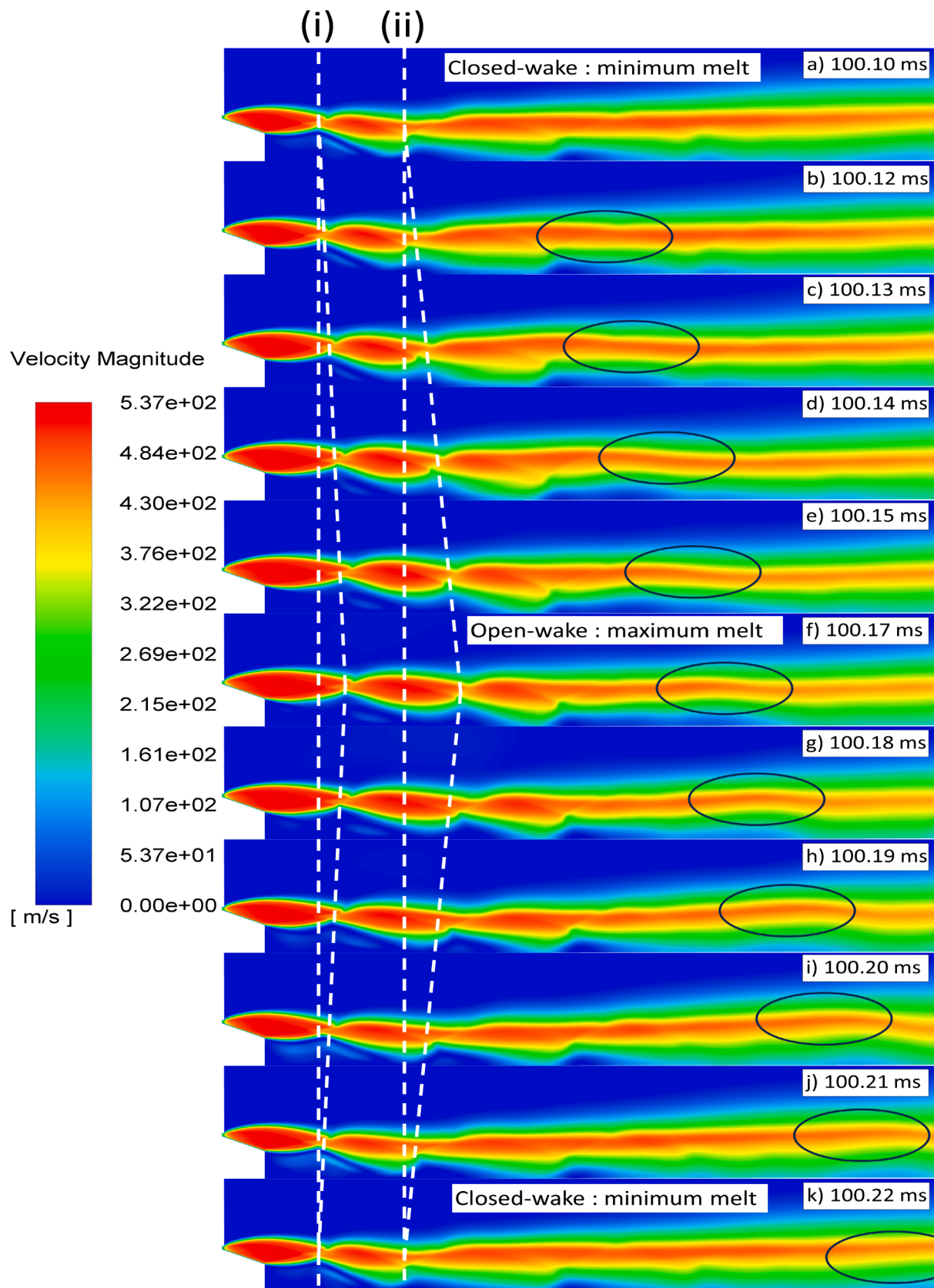
Fig. 23. Flow-field velocity contours of the 4 kg min^{-1} model showing a cycle of the repeated fluctuation seen at t > 100 ms. Two vertical guide-lines (i) & (ii) are fixed at frame a, at the end of first shock-cell and end of second shock-cell, respectively, to compare the extent of fluctuation against other frames. Another two sets of guide-lines are used to trace the movement of the first and second shock-cell ends. The frequency of this fluctuation was found to be 8.3 kHz.

which is less than half of the 2 kg min^{-1} case's frequency of fluctuation. Moreover, no corresponding flow-field fluctuation could be observed for the melt fluctuation of 16.3 kHz of the 4 kg min^{-1} case. Nevertheless, in both the 2 and 4 kg min^{-1} cases, a flow-field fluctuation with a frequency of 20 kHz was evident (2 kg min^{-1} – Fig. 18; 4 kg min^{-1} – Fig. 21), irrespective of whether the flow-field is alternating in wake condition or not; in the case of 2 kg min^{-1} the fluctuation was persistent for the remainder of the simulation, in 4 kg min^{-1} case it existed temporarily at 50 < t < 85 ms. Moreover, it was observed that after the damping out of the initial fluctuation, the onset of the continuous flow-field fluctuation always started gradually and grew with time. Also, two modes of fluctuations were observed: transverse type fluctuation (Fig. 21) and fluctuation in the axial direction (Fig. 23). Considering the continuous flow-field fluctuation in 2 kg min^{-1} and 4 kg min^{-1} cases, it is evident that only 4 kg min^{-1} contains definite and sizeable fluctuations both in melt in-flow and in the gas flow-field, whereas for 2 kg min^{-1} case, even though it displays continuous flow-field fluctuations, the melt in-flow is highly stable. However, this phenomenon of continuous flow-field fluctuation remains uncertain, with the cause attributed to negligible melt fluctuation seen at t > 65 ms, not yet understood.

Examining the flow-fields against the local maxima and local minima of the melt fluctuation undergoing wake alternation for the 4 kg min^{-1} case i.e. 8.1 kHz, it is now established that the wake exists as a open-wake at the local maxima of the melt fluctuation and as a closed-wake at local minima. However, as established in the literature, the frequency of pulsation present in a physical atomisation process was said to be from 25 – 50 Hz (Mullis et al., 2007). Interestingly, from this study it was identified that the frequency of fluctuation (8.1 kHz) corresponding to alternating wake is much higher than the experimentally observed value. In addition to this frequency there were also other frequencies i.e. 1.4 kHz and 16.3 kHz, that were present in the melt fluctuation which does not appear to correlate to any wake alternation in the flow-field. The origin and correlation of the 1.4 kHz and 16.3 kHz frequency fluctuation to the flow-field fluctuation is still not clear. Comparing the 8.1 kHz melt fluctuation frequency that is corresponding to the wake alternation with the 25 – 50 Hz which is the frequency of fluctuation obtained during experimental atomisation run, it appears the model can be further improved. This large discrepancy can be due to the absence of surface tension and viscosity which in physical atomisation plays a significant role. Nevertheless, as seen in 4 kg min^{-1} case in Fig. 20c-f due to the increased mass loading, the melt present towards outer layer i.e. melt present radially towards due to pre-filming interacted much more strongly with the gas jet, whereas the melt towards the atomiser's axis i. e. melt core travelled downstream without much interaction with the gas jet. This might mean that the melt present in the outer layers, strongly interacting with the gas jet would undergo finer atomisation compared to the melt that is present in the melt core, and this might possibly be an explanation to why there is a wide particle size distribution in the yield. Furthermore, the GMR value of 1–1.52 observed from the 4 kg min^{-1} case, was distinctly different to the value 2.84, seen in the literature (Mullis et al., 2013a), where a frequency of 25 – 50 Hz was observed. Nevertheless, from the above study even though the mechanism of wake alternation is observed, and the melt undergoes significant pulsation at higher mass flow rates, their corresponding fluctuations were periodic and highly regular, making it far from type of process seen in the physical atomisation process. Moreover, the study also confirms the postulates of Ting, 2003 that in an atomisation process, the introduction of the melt causes continuous wake alternation. The model can be further enhanced by incorporating the melt temperature to replicate the temperature of the melt in its molten state.

5. Conclusion

A 2D axisymmetric annular-slit gas atomiser was analysed as a multiphase flow using commercial CFD code ANSYS Fluent. The simulation focussed on the melt and flow-field variations present in the

model caused by the gas–melt interactions. It was found at lower mass flow rate of 1 kg min^{-1} the gas flow–field by itself is highly stable and requires increased mass loading to disturb it from its steady state condition, and was confirmed in the higher mass loading cases, 2 and 4 kg min^{-1}. From the three different cases, 1, 2 and 4 kg min^{-1} with GMR values 5.5, 2.6, and 1.32 respectively, it was evident there exists multi-layered frequencies modulated onto each other. The model having GMR value 5.5 was gas dominated, exhibiting fluctuations of low and high frequency present in amplitude modulation. For the cases with GMR 2.6 and 1.32, three different levels of frequency of fluctuation were observed – low, mid and high. Through FFT analysis the frequencies of fluctuation were obtained for both cases; 1.4 kHz, 9 kHz, and 19.7 kHz for GMR of 2.6 (2 kg min^{-1}), and 1.4 kHz, 8.1 kHz, and 16.3 kHz for GMR of 1.32 (4 kg min^{-1}). In the case with GMR of 2.6, the high frequency melt fluctuations of 19.7 kHz corresponded flow-field fluctuations, alternating between open- and closed-wake condition. Nevertheless, the wake alternation did not result in any fluctuation in the melt flow rate. However, in the case with GMR of 1.32, the mid-frequency of 8.1 kHz corresponded to the alternating flow-field fluctuations, and also exhibiting significant melt pulsation. The local maxima of the melt fluctuation corresponded to an open-wake condition, and the local minima corresponded to a closed-wake condition. By confirming the presence of a pulsating flow-field which continuously alternates between closed-wake and open-wake, this numerical simulation supports the postulates of Ting, 2003. The model can be further enhanced by extending it to a full 3D model, incorporating surface tension, viscosity, and melt temperature to depict the temperature of the melt in its molten state, to further understand the phenomena in-depth.

CRediT authorship contribution statement

Jo Samuel J: Writing – review & editing, Writing – original draft, Visualization, Validation, Methodology, Investigation, Formal analysis, Data curation, Conceptualization. **Andrew M Mullis:** Supervision. **Duncan J Borman:** Supervision.

Declaration of competing interest

The authors declare that they have no known competing financial interests or personal relationships that could have appeared to influence the work reported in this paper.

Data availability

Data will be made available on request.

References

Amatriain, A., Urionabarrenetxea, E., Avello, A., Martín, J.M., 2022. Multiphase model to predict particle size distributions in close-coupled gas atomization. Int. J. Multiph. Flow 154, 104138.

Anderson, I., Figliola, R., Morton, H., 1991. Flow mechanisms in high pressure gas atomization. Mater. Sci. Eng. A 148, 101–114.

Anderson, I.E., White, E.M.H., Dehoff, R., 2018. Feedstock powder processing research needs for additive manufacturing development. Curr. Opin. Solid State Mater. Sci. 22, 8–15.

Ashokkumar, A.P., 2020. Computational Modelling of Close-Coupled Gas Atomization. University of Leeds, PhD Doctoral theis.

Bigg, T., Mullis, A., 2020. Spatially resolved velocity mapping of the melt plume during high-pressure gas atomization of liquid metals. Metall. Mater. Trans. B 51, 1973–1988.

Buelow, N.L., 2005. Microstructual investigation of mixed rar earth iron boron processed vis melt-spinning and high-pressure gas-atomization for isotrophic bonded permanent magnets. Ames Lab, Ames, IA (United States).

Duangkhamchan, W., Ronsse, F., Depypere, F., Dewettinck, K., Pieters, J., 2012. CFD study of droplet atomisation using a binary nozzle in fluidised bed coating. Chem. Eng. Sci. 68, 555–566.

Guo, K.-K., Chen, J., Shang, S., Liu, C.-S., 2020. Numerical simulation of atomization process of nickel-based alloy powders prepared by vacuum induction melting gas atomization. Vibroengineering PROCEDIA 32, 185–189.

Kaiser, R., Li, C., Yang, S., Lee, D., 2018. A numerical simulation study of the path-resolved breakup behaviors of molten metal in high-pressure gas atomization: With emphasis on the role of shock waves in the gas/molten metal interaction. Adv. Powder Technol. 29, 623–630.

Luo, S., Wang, H., Gao, Z., Wu, Y., Wang, H., 2021. Interaction between high-velocity gas and liquid in gas atomization revealed by a new coupled simulation model. Mater. Des. 212, 110264.

Luo, S., Ouyang, Y., Wei, Q., Lai, S., Wu, Y., Wang, H., Wang, H., 2023. Understanding the breakup behaviors of liquid jet in gas atomization for powder production. Mater. Des. 227, 111793.

McCarthy, I.N., Adkins, N.J., Aslam, Z., Mullis, A.M., Cochrane, R.F., 2013. High speed imaging and Fourier analysis of the melt plume during close coupled gas atomisation. Powder Metall. 52, 205–212.

Morsi, S., Alexander, A., 1972. An investigation of particle trajectories in two-phase flow systems. J. Fluid Mech. 55, 193–208.

Motaman, S., Mullis, A.M., Cochrane, R.F., McCarthy, I.N., Borman, D.J., 2013. Numerical and experimental modelling of back stream flow during close-coupled gas atomization. Comput. Fluids 88, 1–10.

Motaman, S., Mullis, A.M., Cochrane, R.F., Borman, D.J., 2015. Numerical and experimental investigations of the effect of melt delivery nozzle design on the open- to closed-wake transition in closed-coupled gas atomization. Metall. Mater. Trans. B 46, 1990–2004.

Mullis, A., Cochrane, R., Aslam, Z., McCarthy, I., Adkins, N., 2007. High-frame-rate analysis of spray cone geometry during close-coupled gas atomization. Adv. Powder Metall. Part. Mater. 1, 02.

Mullis, A.M., Cochrane, R.F., McCarthy, I.N., Adkins, N.J., 2013a. Log-normal melt pulsation in close-coupled gas atomization. Metall. Mater. Trans. B 44, 789–793.

Mullis, A.M., Farrell, L., Cochrane, R.F., Adkins, N.J., 2013b. Estimation of cooling rates during close-coupled gas atomization using secondary dendrite arm spacing measurement. Metall. Mater. Trans. B 44, 992–999.

Shi, Y., Lu, W., Sun, W., Zhang, S., Yang, B., Wang, J., 2022. Impact of gas pressure on particle feature in Fe-based amorphous alloy powders via gas atomization: Simulation and experiment. J. Mater. Sci. Technol. 105, 203–213.

Ting, J., 2003. A Pulsatile Atomization Model. In: In 41st Aerospace Sciences Meeting and Exhibit, p. 1283.

Ünal, R., Aydin, M., 2007. High efficient metal powder production by gas atomisation process. Mater. Sci. Forum 534–536, 57–60.

Wang, P., Liu, J., Dong, Y., Zhu, Z., Pang, J., Zhang, J., 2023. Breakup process modeling and production of FeSiAl magnetic powders by close-coupled gas atomization. J. Mater. Res. Technol. 23, 730–743.

Wang, P., Zhou, X.-L., Li, X.-G., Chen, Z.-P., Hu, Q.-P., Wang, X., Yu, Z.-Y., 2024. Numerical and experimental investigation of close-coupled twin-nozzle gas atomization towards fine high-entropy alloy powder production. J. Mater. Process. Technol. 324, 118238.

Xu, L., Zhou, X., Li, J., Hu, Y., Qi, H., Wen, W., Du, K., Ma, Y., Yu, Y., 2020. Numerical simulations of molten breakup behaviors of a de laval-type nozzle, and the effects of atomization parameters on particle size distribution. Processes 8, 1027.

Yule, A.J., Dunkley, J.J., 1994. Atomization of melts for powder production and spray deposition. Clarendon Press.

Zeoli, N., Gu, S., 2006. Numerical modelling of droplet break-up for gas atomisation. Comput. Mater. Sci 38, 282–292.

Zeoli, N., Gu, S., 2008. Computational simulation of metal droplet break-up, cooling and solidification during gas atomisation. Comput. Mater. Sci 43, 268–278.

Zhao, X., Xu, J., Zhu, X., Zhang, S., 2009. Effect of atomization gas pressure variation on gas flow field in supersonic gas atomization. Sci. China Ser. E: Technol. Sci. 52, 3046–3053.